Estimates of Black Carbon Emissions in the Western United States Using the GEOS-Chem Adjoint model

Yuhao Mao[1,2,3], Qinbin Li[1,2], Daven K. Henze[4], Zhe Jiang[5*], Dylan B. A. Jones[5,2], Monika Kopacz[6], Cenlin He[1,2], Ling Qi[1,2], Mei Gao[1,2], Wei-Min Hao[7], Kuo-Nan Liou[1,2]

[1]Department of Atmospheric and Oceanic Sciences, University of California, Los Angeles, CA 90095, USA

[2]Joint Institute for Regional Earth System Science and Engineering, University of California, Los Angeles, CA 90095, USA

[3]State Key Laboratory of Atmospheric Boundary Layer Physics and Atmospheric Chemistry, Institute of Atmospheric Physics, Chinese Academy of Sciences, Beijing, 100029, China

[4]Department of Mechanical Engineering, University of Colorado, Boulder, CO 80309, USA

[5]Department of Physics, University of Toronto, Toronto, ON M5S 1A7, Canada

[6]NOAA Climate Program Office, Silver Spring, Maryland, 20910, USA

[7]Fire Sciences Laboratory, U.S. Forest Service, Missoula, MT, 59808, USA

[*]Now at Jet Propulsion Laboratory, California Institute of Technology, Pasadena, CA, 91109, USA

**Corresponding author address*: Q. B. Li (qli@atmos.ucla.edu)

Abstract

We estimate black carbon (BC) emissions in the Western United States for July–September 2006 by inverting surface BC concentrations from the Interagency Monitoring of PROtected Visual Environment (IMPROVE) network using a global chemical transport model (GEOS-Chem) and its adjoint. Our best estimate of the BC emissions is 49.9 Gg at 2 °×2.5 ° (a factor of 2.1 increase) and 47.3 Gg at 0.5 °×0.667 ° (1.9 times increase). Model results now capture the observed major fire episodes with substantial bias reductions (~35% at 2 °×2.5 ° and ~15% at 0.5 °×0.667 °). The emissions are ~20–50% larger than those from our earlier analytical inversions (Mao et al., 2014). The discrepancy is especially drastic in the partitioning of anthropogenic versus biomass burning emissions. The August biomass burning BC emissions are 4.6–6.5 Gg and anthropogenic BC emissions 8.6–12.8 Gg, varying with the model resolution, error specifications, and subsets of observations used. On average both anthropogenic and biomass burning emissions in the adjoint inversions increase twofold relative to the respective *a priori* emissions, in distinct contrast to the halving of the anthropogenic and tripling of the biomass burning emissions in the analytical inversions. We attribute these discrepancies to the inability of the adjoint inversion system, with limited spatiotemporal coverage of the IMPROVE observations, to effectively distinguish collocated anthropogenic and biomass burning emissions on model grid scales. This calls for concurrent measurements of other tracers of biomass burning and fossil fuel combustion (e.g., carbon monoxide and carbon isotopes). We find that the adjoint inversion system as is has sufficient information content to constrain the total emissions of BC on the model grid scales.

1. Introduction

Black carbon (BC) is directly emitted from the incomplete combustion of carbonaceous fuels (Bond et al., 2004). Black carbon has substantial impacts on global climate because of its strong absorption of solar radiation (e.g., Horvath, 1993; Ramanathan and Carmichael, 2008), important influences in cloud processes (Jacobson, 2006), and significant impacts on snow and ice albedos (Flanner et al., 2007, 2009). The radiative forcing due to BC is 0.64 W m^{-2} globally (IPCC, 2013), ranked as the third-biggest human cause of global warming. Black carbon is also known as an important agent to both degrade air quality and affect human health (McMurry et al., 2004; Anenberg et al., 2011, 2012). Because of its shorter lifetime relative to long-lived greenhouse

gases, BC reduction may provide an efficient near-term solution to mitigate global warming and to improve air quality and public health simultaneously (Ramanathan and Carmichael, 2008; Bond et al., 2013).

The deposition of BC on glaciers is known to be an important driver to the observed rapid glacier retreat (Xu et al., 2009; Painter et al., 2013) and further impacts the regional hydrological cycle over mountain ranges (Qian et al., 2009). In the Western United States (WUS), mountain snowmelt accounts for at least 70% of the annual stream flow (Qian et al., 2009). In the recent decades, the WUS is experiencing the most severe drought (e.g., Melillo et al., 2014) and the water level of the Colorado River has been decreasing (e.g., Vano et al., 2013). It is thus imperative to better understand the sources, transport, and deposition of BC in the WUS mountain ranges.

Recent studies have shown that the biomass burning BC emissions in the WUS were underestimated by a factor of two in both the absolute magnitudes and the timing and location of the emissions (Mao et al., 2011, and references therein). The large uncertainty is partially because previous burned area algorithms lacked the ability to detect small fires (Giglio et al., 2010; Randerson et al., 2012). Long-term records have shown an increase in fires in terms of both fire frequency and burned area in the WUS over the past 30 years because of the rising spring and summer temperatures (Westerling et al., 2006; Peterson and Marcinkowski, 2014; Jin et al., 2014) and increasing urbanization (e.g., Cannon and DeGraff, 2009). This upward trend is expected to continue as a result of the warming climate (Spracklen et al., 2009; Yue et al., 2013). Biomass burning emissions will conceivably have an even larger contribution to BC in the WUS in this century, especially considering that North American anthropogenic emissions have been steadily decreasing as a result of effective emission controls (Novakov et al., 2003; Bond et al., 2007; Ramanathan and Carmichael, 2008).

Knowledge of the emissions of a chemical species is imperative for better understanding of its transport, distribution, and removal. Traditional bottom-up emission estimates generally depend on emission factors using socioeconomic, energy, land use, or environmental data (Bond et al., 2007, 2013; Lu et al., 2011). Inverse modeling is able to improve the bottom-up emission estimates by minimizing an error-weighted least squares cost function (Rodgers, 2000). There are two methods to achieve the minimum of the cost function, the so-called analytical inversion and adjoint (i.e. variational) inversion (Kopacz et al., 2009, and references therein). The

analytical method obtains an analytical solution by explicitly constructing a Jacobian matrix. However, the analytical method limits the number of the observations and the number of the sources and source regions that could be optimized because it is computationally expensive. Alternatively, the adjoint method seeks a numerical solution iteratively by using a suitable optimization algorithm (e.g., the conjugate gradient method) and is thus able to handle a very large number of observations and a large state vector resolved on a model grid scale.

Inverse modeling in general is suited for estimating emissions of unreactive or weakly reactive chemical species when their atmospheric concentrations are linearly or weakly non-linearly dependent on emissions (Müller and Stavrakou, 2005). These species include but are not limited to carbon dioxide (e.g., Gloor et al., 1999; Chevallier et al., 2007; Pickett-Heaps et al., 2011), methane (e.g., Hein et al., 1997; Meirink et al., 2008; Wecht et al., 2012), and carbon monoxide (CO) (Stavrakou and Müller, 2006; Arellano et al., 2004, 2006, 2007; Chevallier et al., 2009; Jones et al., 2009). Despite the non-linear complexities of the inversion system for short-lived tracer species, several studies have attempted to constrain emissions for nitrogen oxides (e.g., Martin et al., 2003, 2006; Chai et al., 2009; Lin et al., 2010; Zyrichidou et al., 2013), sulfur dioxide (Lee et al., 2012), and ammonia (Zhu et al., 2013; Paulot et al., 2014). The inverse method has also been used to constrain emission fluxes of aerosols, for instance, inorganic particulate matter (Henze et al., 2009; Xu et al., 2013) and dust (Yumimoto et al., 2008; Wang et al., 2012).

A number of modeling studies have attempted to constrain and attribute BC emissions on regional to continental scales. Several studies have used multiple regressions to estimate annual mean emissions of primary carbonaceous aerosols in the U.S. (Park et al., 2003) and in China (Fu et al., 2012; Wang et al., 2013). A global chemical transport model (CTM) and its adjoint was used to attribute the source regions of BC in the Himalayas and the Tibetan Plateau (Kopacz et al., 2011). Anthropogenic and biomass burning emissions of BC during the Asian Pacific Regional Aerosol Characterization Experiment (ACE-Asia) (Huebert et al., 2003; Seinfeld et al., 2004) were estimated using a continental-scale CTM (stretched over the Pacific basin) and its adjoint (Hakami et al., 2005). Previously, linear analytical inversions were applied to optimize sources and source regions (the Rockies, California and the Southwest, and the Pacific Northwest) of BC in the WUS for May-October 2006 (Mao et al., 2014). The analytical

inversions show factors of 3–5 increase of the biomass burning emissions and a ~50% reduction of the anthropogenic emissions, relative to the corresponding *a priori* (Mao et al., 2014).

Here we apply the adjoint inversion method (Henze et al., 2007, 2009) to improve estimates of BC emissions in the WUS (defined hereinafter as 30°–50°N, 100°–125°W) on model grid scales by inverting the surface BC concentrations from the Interagency Monitoring of PROtected Visual Environment (IMPROVE, Malm et al., 1994) network using the GEOS-Chem global 3-D CTM and its adjoint. We use the observations for 2006 from 69 mostly mountainous sites in the WUS (Fig. 1). We focus our analysis on biomass burning emissions during the large fire season of July–September in the region (Mao et al., 2011, 2014).

2. GEOS-Chem and its adjoint

We apply the GEOS-Chem global 3-D CTM (Bey et al., 2001; with many updates thenceforth) to analyze IMPROVE BC data. Here we use GEOS-Chem version 8-02-01 (available at http://geos-chem.org) driven by GEOS-5 meteorological data. The detailed model configurations are as discussed by Mao et al. (2011, 2014). Global annual anthropogenic emissions of BC are from Bond et al. (2007). Seasonal variations of anthropogenic emissions are considered over the U.S. following Park et al. (2003). Biomass burning emissions of BC are from the Global Fire Emissions Database version 2 (GFEDv2) (Randerson et al., 2007; van der Werf et al., 2006), with improved spatiotemporal distributions using the active fire counts from the Moderate Resolution Imaging Spectroradiometer (MODIS) (Mao et al., 2014). For computational expediency, we conduct 'offline' simulations of carbonaceous aerosols (Mao et al., 2011, and references therein) for 2006 at both 2°×2.5° (globally) and 0.5°×0.667° (nested over North America, 40°–140°W longitudes, 10°–70°N latitudes, cf. Fig. 1 in Wang et al., 2004) horizontal resolutions, following Mao et al. (2014). The first three months are used for initialization and we focus our analysis on July–September. Model results are sampled at the corresponding location and time of IMPROVE observations.

We use the GEOS-Chem adjoint (Henze et al., 2007, 2009) to estimate BC emissions in the WUS. A particular type of application of the adjoint is source attribution of chemical species at individual sites (e.g., Zhang et al., 2009; Kopacz et al., 2011; Parrington et al., 2012; Walker et al., 2012). Here we use the adjoint of the "offline" simulation of BC at 2°×2.5° (globally) and 0.5°×0.667° (nested over North America, Jiang et al., 2015a). The computational cost of the

adjoint simulation is 50% greater than that of the corresponding forward simulation. We validate the adjoint simulation of BC by comparing the adjoint gradients and the forward model sensitivities calculated using finite difference approximation (Henze et al., 2007; Zhu et al., 2013):

$$\wedge = \frac{J(\sigma + \delta\sigma) - J(\sigma)}{\delta\sigma} \quad (1)$$

where J is the cost function (Mao et al., 2014, and references therein), as discussed below in Sect. 3.1, and σ the scaling factor of BC emissions. We use here $\delta\sigma$ = 0.1, following Henze et al. (2007). Specifically we calculate the sensitivity of the BC mass at the surface with respect to the scaling factors of biomass burning and anthropogenic emissions of BC. Fig. S1 shows the results from 1-week simulations for biomass burning (top panel) and anthropogenic emissions (bottom panel) for August 2006. The adjoint and finite difference sensitivities are in excellent agreements ($r \approx 1$), reaffirming the accuracy of the adjoint code.

3. Inversion approach

3.1 The adjoint solution to the inverse problem

Consider the general problem of inferring emissions (state vector $\boldsymbol{X}$) from a set of given observations (observation vector $\boldsymbol{Y}$) with error $\boldsymbol{\varepsilon}$. They are related via a forward model F as follows (Rodgers, 2000):

$$\boldsymbol{Y} = F(\boldsymbol{X}, b) + \varepsilon \quad (2)$$

where $\boldsymbol{X}$ are the monthly biomass burning or anthropogenic emissions of BC in each model grid box in the present study, $\boldsymbol{Y}$ the 24-hour average surface BC concentrations from the 69 IMPROVE sites (Fig. 1), b the model variables not directly retrieved from the inversion, F the GEOS-Chem model, and ε the observation error (measurement and forward model errors). Based on Bayes' theorem and the assumption of Gaussian error distributions (Rodgers, 2000), the optimal or Maximum *A Posteriori* (MAP) solution for $\boldsymbol{X}$ given $\boldsymbol{Y}$ is equivalent to finding the minimum of a cost function $J(\boldsymbol{X})$:

$$J(\boldsymbol{X}) = \frac{1}{2}\gamma_r(\boldsymbol{X} - \boldsymbol{X}_\mathrm{a})^\mathrm{T}\mathbf{S}_\mathrm{a}^{-1}(\boldsymbol{X} - \boldsymbol{X}_\mathrm{a}) + \frac{1}{2}\sum_{i=0}^{N}[\boldsymbol{Y}_i - F(\boldsymbol{X}_i)]^\mathrm{T}\mathbf{S}_\varepsilon^{-1}[\boldsymbol{Y}_i - F(\boldsymbol{X}_i)] = \gamma_r J_b + J_o \quad (3)$$

where $\boldsymbol{X}_\mathrm{a}$ and $\mathbf{S}_\mathrm{a}$ are the *a priori* emissions and the associated error covariance, $\mathbf{S}_\varepsilon$ the observational error covariance, and γ_r the regularization parameter that adjusts the relative

constraints by the observation term (i.e., the prediction term, J_o) and the background term (i.e., the penalty term, J_b) of the cost function (Hakami et al., 2005; Müller and Stavrakou, 2005; Henze et al., 2007; Kopacz et al., 2009). An observation term is added to the cost function for each additional data source during the time interval [t_0, t_N].

The adjoint approach seeks to minimize the cost function $J(\boldsymbol{X})$ numerically and iteratively rather than analytically (Henze et al., 2007, 2009). Starting from an initial guess (i.e., the *a priori* emissions), the adjoint model efficiently computes the cost function gradients. A quasi-Newton L-BFGS algorithm (Liu and Nocedal, 1989) is then used to minimize the cost function iteratively, taking as input the cost function and its gradient. Such iterative optimizations using GEOS-Chem and its adjoint have been discussed in details previously (Henze et al., 2007, 2009; Kopacz et al., 2009, 2010).

3.2 Error specifications

A key aspect of inverse modeling is the specification of the error covariance matrices of variable parameters and observations (Palmer et al., 2003; Heald et al., 2004). We set the *a priori* and observation errors following Mao et al. (2014). We assume for separate inversions presented here an uncertainty of 30, 50, or 200% for anthropogenic BC emissions and 300 or 500% for biomass burning BC emissions. We assume that the *a priori* errors are spatially uncorrelated. The spatial correlations between the *a priori* errors have been proved to improve the inversion, particularly in regions adjacent to strong sources and less directly constrained (Stavrakou and Müller, 2006). For example, the assumption of no spatial correlation between *a priori* errors would underestimate the biomass burning emissions in regions close to the extensive agriculture fires. We set the observation error at 30, 50, or 100%, which includes the model, representation, and measurement errors. Setting these errors in relative terms can become problematic when the observed BC concentrations are vanishingly small. These small values tend to skew the inversion toward matching the minimal errors. We thus set an absolute error of 0.04 μg m^{-3} based on the estimated observation errors. We showed previously that the combination of 50% uncertainty for anthropogenic emissions, 500% uncertainty for biomass burning emissions, and 30% total observation error provided the best retrieval results in the analytical inversions (Mao et al., 2014). We adopt this set of error specifications in the standard inversion in the present study (Case 1, Table 1). The results are compared with those from the analytical inversions of Mao et al. (2014).

3.3 Emission scaling factors $\boldsymbol{X}/\boldsymbol{X}_a$

We optimize here the scaling factors of emissions $\boldsymbol{X}/\boldsymbol{X}_a$ (rather than the actual emissions $\boldsymbol{X}$), as a standard practice in adjoint inversion studies (Henze et al., 2009). The form of the scaling factors in an adjoint inversion is crucial for the inversion to efficiently and rapidly converge to a solution (Jiang et al., 2015b). When the optimization is directly on the scaling factors expressed linearly as $\boldsymbol{X}/\boldsymbol{X}_a$ (i.e., the cost function gradient is computed with respect to $\boldsymbol{X}/\boldsymbol{X}_a$), the regions with strong *a priori* emissions tend to dominate the optimization, manifested in unrealistically large changes of emissions in these regions but limited variations in the regions with weak *a priori* emissions. Alternatively, when the optimization is instead on the logarithm of the scaling factors, $\ln(\boldsymbol{X}/\boldsymbol{X}_a)$ (i.e., the cost function gradient is now computed with respect to $\ln(\boldsymbol{X}/\boldsymbol{X}_a)$), the optimization can potentially result in an unbalanced convergence that is much faster for the regions with positive biases than for the regions with negative biases. Here we calculate cost function gradients with a hybrid form of scaling factors (Jiang et al., 2015b),

$$gradients = \begin{cases} \dfrac{x}{x_a} \le 1 & \dfrac{\partial J}{\partial \ln(x/x_a)} = \dfrac{\partial J}{\partial x} \times x_a \times \dfrac{x}{x_a} \\ \dfrac{x}{x_a} > 1 & \dfrac{\partial J}{\partial \dfrac{1}{2}\left[(x/x_a)^2 - 1\right]} = \dfrac{\partial J}{\partial x} \times x_a / \dfrac{x}{x_a} \end{cases} \quad (4)$$

so that the resulting optimization converges equally efficiently for the regions with positive or negative biases.

3.4 The regularization parameter γ_r

The assumption that a priori errors are spatially uncorrelated hinges on the consideration that the spatial resolution of the CTM is much larger than the correlation length scale of the individual emission sources (Henze et al., 2009). However, the uncertainties of emissions from different model grid boxes (e.g., ~200×250 km^2 at 2°×2.5°) within a region (e.g., a country) are usually correlated (Stavrakou and Müller, 2006). Without explicitly enforcing these correlations, a regularization parameter, which ensures a smooth solution to the inversion, is often used to rectify the aforementioned inconsistency, by ensuring the *a posteriori* emissions remain sufficiently close to the *a priori* values, which themselves reflect such correlations owing to the nature of bottom-up emissions inventories (Rodgers, 2000; Henze et al., 2009). Here we use the regularization parameter γ_r to balance the two terms of the cost function (Eq. 3) (Hakami et al.,

2005; Müller and Stavrakou, 2005; Henze et al., 2007; Kopacz et al., 2009). A large γ_r relaxes the solution toward the *a priori* constraint while limiting the influence of the observation term, resulting in over-smoothing of the solution. In contrast, a small γ_r largely curtails the influence of the *a priori* constraint. To find an optimal γ_r value, we conduct inversions with a range of γ_r (10, 1, 0.1, 0.01, 0.001, and 0.0001). The resulting *a posteriori* cost function values, normalized by the initial value, are shown in Fig. S2 (top). We use $\gamma_r = 0.001$ in the analysis hereinafter, as that provides a small normalized *a posteriori* cost function and a sufficient cost function reduction.

As an example, Fig. S2 (bottom) shows the cost function reduction for August 2006. We regard the minimization as having converged sufficiently when the cost function changes less than 2% during the last three iterations. The cost function converges in 10–20 iterations (35% reduction at $2° \times 2.5°$ and 50% at $0.5° \times 0.667°$). The cost function values are of the same order as the number of observations used in the inversion (~690). The penalty term (Sect. 3.1) is a mere 3% of the *a posteriori* cost function at $2° \times 2.5°$ and 8% at $0.5° \times 0.667°$, therefore the influence of the *a priori* is likely rather modest.

4. Results and discussion

Our standard adjoint inversion is at $2° \times 2.5°$, with uncertainties of 50% for anthropogenic emissions, 500% for biomass burning emissions, and 30% for the observation (Case 1, Table 1). The *a posteriori* emissions are 49.9 Gg at $2° \times 2.5°$ and 47.3 Gg at $0.5° \times 0.667°$ for July–September, substantially higher than the *a priori* (24.3 Gg), because the modeled surface BC concentrations are largely biased low at most IMPROVE sites (Mao et al., 2011, 2014).

We focus our discussions hereinafter on August only, unless stated otherwise, for the sake of concision and clarity. Fig. 2 shows the *a priori* and the *a posteriori* monthly anthropogenic and biomass burning BC emissions from the standard adjoint inversion for August. The anthropogenic and biomass burning emissions are adjusted (higher or lower) alike in most grid boxes. Both the anthropogenic and biomass burning emissions increase twofold overall. The biomass burning emissions increase by varying factors (Table 1): 2.3 in the Rockies, 2.8 in California and the Southwest, and 1.5 in the Pacific Northwest – the regions are defined as in Mao et al. (2014).

The sensitivity of the cost function $J(\boldsymbol{X})$ to the BC emissions is a useful metric for evaluating the inversions. Following Henze et al. (2009), we normalize the sensitivity as follows,

$$\frac{\partial J(\boldsymbol{X})}{\partial x_{m,i}} \frac{x_{m,i}}{J(\boldsymbol{X})} \quad (5)$$

It is the percentage of the cost function response to the fractional change in the BC emission source *m* (biomass burning, anthropogenic or total emissions) in model grid box *i*. As such, negative sensitivities are regions in which the model underestimates actual emissions and an increase of BC emissions would improve model agreement with the observations. It is the opposite for positive sensitivities. The results for August are shown in Fig. 3. The largest negative sensitivities to biomass burning emissions are in Washington, Ohio, Idaho, and California, where the model severely underestimates the biomass burning emissions and the sensitivities decrease significantly after the inversions. The inversions generally result in large reductions to both the positive and negative sensitivities (~90% on average at $2°\times2.5°$ and $0.5°\times0.667°$).

4.1 Sensitivity analyses

Here we examine the sensitivity of the adjoint inversions to error specifications, choice of observations, collocated emissions, and the model resolution. These sensitivity analyses also provide a measure of the robustness of the inversions (Mao et al., 2014). For that purpose we conduct adjoint inversions at $2°\times2.5°$ and $0.5°\times0.667°$ (Cases 2–8, Table 1) in addition to the standard inversion (Case 1), with assorted *a priori* and observation errors, different subsets of the IMPROVE data, and collocated anthropogenic and biomass burning emissions. The results are compared and contrasted with those from the standard adjoint inversion in the discussions hereafter, unless stated otherwise. We find that the inversions generally show comparable and consistent results with those from the standard inversion. The ensemble *a posteriori* biomass burning emissions (Cases 1–8) are 4.6–6.5 Gg (a factor of 1.7–2.3 relative to the *a priori*) and anthropogenic emissions 8.6–12.8 Gg (a factor of 1.5–2.2 increase).

4.1.1 Error specifications

We first conduct adjoint inversions (Cases 2–5) to examine the sensitivity of the inversions to the *a priori* and observation errors. The *a posteriori* emissions are 3% lower when we reduce the

uncertainty of the *a priori* biomass burning emissions from 500 to 300% (Case 2). Reducing the uncertainty of the *a priori* anthropogenic emissions from 50 to 30% brings no appreciable change to the *a posteriori* emissions (Case 3). Quadrupling that uncertainty (from 50 to 200%) increases the *a posteriori* emissions by 10% (Case 4). We find that the inversions are more sensitive to the observation error than the *a priori* error. For instance, an increase from 30 to 100% of the observation error (Case 5) results in a 16% decrease in the *a posteriori* emissions.

4.1.2 Choices of observations

A robust inversion critically relies on the spatiotemporal coverage of the observations. For carbon dioxide, a minimum of 10 sites per region were needed in analytical inversions (Gloor et al., 1999). For BC, the number of site is usually smaller. Only ~1000 BC observations were used to optimize ~20000 variables in an adjoint study (Hakami et al., 2005) during ACE-Asia (Huebert et al., 2003; Seinfeld et al., 2004). In this study, we use ~690 observations to constrain ~600 variables at 2 °×2.5 ° and ~10000 at 0.5 °×0.667 °.

Here we conduct two inversions to probe the sensitivity of the inversion to observations by using subsets of the IMPROVE data and comparing the results with those from the standard inversion (Case 1). In the inversion (Case 6), we set aside 13 (~20% of the 69) sites with $\chi^2 > 1.5$ and large model-observation departure (> 0.5 μg m^{-3}). χ^2 is calculated as the square of the ratio of the difference between modeled and observed surface BC concentrations to the observation accuracy. The measurements from these 13 sites are used as independent observations, whereas the measurements from the remaining 56 sites are used in the inversion. We find that the resulting *a posteriori* emissions (Fig. 4) are within 6% of those from Case 1 (Fig. 2). The emissions differ significantly only in ~10% of the grid boxes, mainly in the Pacific Northwest and the Rockies. The resulting surface BC concentrations averaged over the 13 sites are within 15% between the two Cases. There is a ~15% reduction in the mean bias of the surface BC concentrations (averaged over the 13 sites) for Case 6 and 20% for Case 1. In another inversion (not shown), we set aside four (~5% of the 69) sites with $\chi^2 > 2$. The results are also consistent with those from Case 1.

4.1.3 Collocated emissions

In the WUS mountain ranges, biomass burning BC emissions are substantially underestimated (Mao et al., 2011). There are large uncertainties in the temporal variation and spatial distribution of fire emissions (Langmann et al., 2009). Small fires are likely a major source of these uncertainties (Randerson et al., 2012). For instance, small fires can lead to large relative errors (50–100%) in burned area estimates (Korontzi et al., 2006; Giglio et al., 2006, 2010; McCarty et al., 2009; Roy and Boschetti, 2009).

Fig. 5 shows monthly anthropogenic and biomass burning emissions in each $2° \times 2.5°$ model grid box in the WUS. Collocated anthropogenic and biomass burning emissions are in most of the grid boxes. The anthropogenic emissions are larger than the biomass burning emissions in 80% of the grid boxes and still significant in the remaining 20%. Here we conduct two inversions (Cases 7–8) to examine the ability of the adjoint inversion system to distinguish collocated biomass burning versus anthropogenic emissions, especially in the regions where the biomass burning emissions are likely underestimated. We conduct one inversion (Case 7) on the total emissions, considering an error of 200% for the *a priori* emissions. We find that the resulting total *a posteriori* emissions increase by a factor of 2.2 relative to the *a priori* and are within 2% of those from Case 1. We conduct another inversion (Case 8) to examine how much the inversion can distinguish the collocated emissions. In each grid box, we add 2.5 Mg (~10% of the maximum emissions among the grid boxes) as a diagnosis to the (*a priori*) biomass burning emissions of BC and examine the degree to which the inversion results change the partitioning of biomass burning versus anthropogenic emissions by comparing the inversion results with those from Case 1 (or Case 7). The differences in the *a posteriori* emissions of BC between Cases 8 and 1 are shown in Fig. 6. The anthropogenic and biomass burning emissions from Case 8 show opposite and disproportional changes, relative to the corresponding emissions from Case 1. Specifically, there is an approximately linear increase (i.e., Case 8 relative to Case 1) in the biomass burning emissions (by more than 5 Mg in nearly every grid box) and a linear decrease (again, Case 8 relative to Case 1) in the anthropogenic emissions (by ~3 Mg, except in California). However, the anthropogenic and biomass burning emissions of BC, when summed over the WUS, each increases twofold (relative to the corresponding *a priori*) in both Cases 8 and 1 – the total emissions remain essentially the same (less than 1% difference) between the two Cases (Table 1). The inversion system tends to overcompensate the deficit of biomass burning emissions by disproportionately increasing anthropogenic emissions instead in the same grid box.

This indicates that the inversion system lacks the ability to effectively distinguish collocated biomass burning and anthropogenic emissions in the WUS on model grid scales.

4.1.4 Model resolution

GEOS-Chem simulations generally provide better agreements with observations at 0.5 °×0.667 ° than at 2 °×2.5 ° for CO (Wang et al., 2004; Chen et al., 2009), ozone (Zhang et al., 2011), mercury (Zhang et al., 2012), and BC (Mao et al., 2014). We found in a companion study (Mao et al., 2014) that the *a posteriori* BC emissions from analytical inversions of the IMPROVE observations were considerably lower at 0.5 °×0.667 ° than at 2 °×2.5 °. Intuitively, the larger smearing of the emissions at the coarser resolution results in larger model-observation discrepancies (Chen et al., 2009). The larger discrepancies in turn tend to drive the inversion system toward imposing larger emissions at the coarser than the finer resolutions when minimizing the said discrepancies.

As a comparison to the standard inversion at 2 °×2.5 ° (Case 1), we conduct another adjoint inversion at 0.5 °×0.667 ° (Case 9) with the same error specifications. The resulting *a posteriori* emissions are shown in Fig. 7. The biomass burning emissions are 53% larger in Case 9 than in Case 1 in the Pacific Northwest but 27% lower in the Rockies and 43% lower in California and the Southwest. The total emissions are considerably lower at 0.5 °×0.667 ° (27% lower for anthropogenic and 10% for biomass burning) yet provide better agreement with the observations (Sect. 4.4). The *a posteriori* emissions from the standard analytical inversion (Mao et al., 2014) are also shown in Fig. 7 for comparison. The differences between the analytical and adjoint inversions (Table 1) are slightly larger at 0.5 °×0.667 ° (53%) than at 2 °×2.5 ° (39%). The larger differences reflect in part that the adjoint inversion system has even more difficulty in constraining the emissions at the finer grid scale (Sects. 4.1.3 and 4.2).

4.2 Pseudo observations

We use pseudo observations of BC concentrations in another group of inversions (Table 2) to further examine the sensitivity of the adjoint inversions to collocated emissions, error specifications, and observations. We generate the pseudo observations by increasing the *a priori* biomass burning emissions of BC in each grid box threefold. The total amount of the *a priori* emissions added is 5.6 Gg. The frequency of the pseudo observations are 24-hour averages for

every three days, following the IMPROVE measurements of BC. We then invert the pseudo observations at $2° \times 2.5°$ and with the same *a priori* emissions as those used in the standard inversion (Case 1). We examine whether the inversions are able to fully recover the emissions used to generate the pseudo observations. Specifically, we expect the *a posteriori* biomass burning emissions to increase threefold relative to the *a priori*, whereas the anthropogenic emissions remain unchanged.

We first conduct two inversions (Pseudos 1–2) to investigate the ability of the adjoint inversion system to distinguish collocated anthropogenic and biomass burning emissions. We consider two extreme scenarios: the pseudo observations are in every surface grid box (Pseudo 1) and in every grid box in the lowest 15 vertical layers (Pseudo 2). Other aspects of the two inversions remain the same as those of the standard inversion (Case 1). We find that the results are nearly indistinguishable. The *a posteriori* cost function is greatly reduced (by 95% in Pseudo 1 and by 97% in Pseudo 2). The *a posteriori* emissions both increase by exactly 5.6 Gg, fully recovering the added biomass burning emissions. However, the increase is uneven and not limited to the biomass burning emissions. The biomass burning emissions increase by a factor of 2.3 and anthropogenic emissions by a factor of 1.3. The inversions thus falsely impose larger anthropogenic emissions to minimize the large discrepancies between the model predictions and the pseudo observations.

In the next three inversions (Pseudos 3–5), we examine the sensitivity of the inversion system to the constraints for anthropogenic versus biomass burning emissions. The uncertainty of the anthropogenic emissions is reduced to 10% in Pseudo 3. We assume that the anthropogenic emissions are perfect and leave them unchanged in Pseudo 4. In Pseudo 5, we let the biomass burning emissions remain unaltered. Other aspects of Pseudos 3–5 remain the same as those of Pseudo1. We find that the resulting *a posteriori* emissions from the former two (Pseudos 3 and 4) recover fully the added (biomass burning) emissions. The biomass burning emissions increase by a factor of 2.5 in Pseudo 3 (versus 2.3 in Pseudo 1) and by a factor of 2.9 in Pseudo 4. However, the *a posteriori* emissions from Pseudo 5 increase by only 4.2 Gg, recovering just 75% of the added (biomass burning) emissions.

Concurrent measurements of other combustion tracers, for example, CO and carbon isotopes, can conceivably provide additional information to distinguish collocated BC emissions. Previous studies have shown that the ratio of BC to CO significantly varies with the fuel types and thus is

a good indicator for identifying BC sources (Spackman et al., 2008; Han et al., 2009; Subramanian et al., 2010; Reche et al., 2011). Carbon isotopes such as ^{14}C are known to be present at small and more or less constant levels in biogenic emissions but absent in fossil fuels (Schichtel et al., 2008). Ample studies heretofore have shown that ^{14}C is useful for analyzing the source apportionment of atmospheric carbonaceous aerosols (Heal, 2014, and references therein). ^{14}C measurements are currently only available from short-term studies in part because of the relatively high cost of deploying such measurements in routine monitoring networks (Lewis et al., 2004; Bench et al., 2004, 2007; Szidat et al., 2006).

Additionally, we conduct four inversions (Pseudos 6–9) to examine the minimum number of observation sites needed for the inversions. The inversions are the same as Pseudo 1, except that the pseudo observations are randomly distributed in 75% (Pseudo 6), 50% (Pseudo 7), or 25% (Pseudo 8) of the surface grid boxes, or in the surface grid boxes with larger than 5 fire counts per month (covering ~50% of surface grid boxes, Pseudo 9). The resulting *a posteriori* emissions recover 94% (Pseudo 6), 93% (Pseudo 7), 80% (Pseudo 8), and 93% (Pseudo 9) of the added (biomass burning) emissions. Randomly, surface observations covering at least 50% of the model grid boxes are needed to estimate the total BC emissions on the model grid scale. In our case, 69 IMPROVE sites are used to constrain BC emissions in ~100 surface grid boxes at $2°\times2.5°$ and ~1500 at $0.5°\times0.667°$. As we discussed in Sect. 4.1.2, the differences between the inversion results with 69 or 56 IMPROVE sites are essentially small, indicating that the 69 or 56 sites alone (absent other observations) are likely sufficient only for constraining the total emissions of BC, especially at $2°\times2.5°$. With pseudo observations located at biomass burning source regions (Pseudo 9), the resulting *a posteriori* biomass burning emissions are 5% higher than those from the inversion with similar amount of pseudo observations (in 50% of surface grid boxes, Pseudo 7), whereas the total *a posteriori* emissions are almost unchanged between Pseudos 7 and 9. Thus, pseudo observations located at source regions would be more effective to constrain sources.

4.3 Adjoint versus analytical inversions

The analytical method is limited to constraining emissions over aggregated regions because of computational limitations, whereas the adjoint method is able to describe emission variability on finer scales and more efficiently (Kopacz et al., 2009). There are large differences in the *a*

posteriori emissions between the analytical and adjoint inversions, not only in the spatial distributions but also in the magnitudes (Figs. 5 and 10). In California, for example, the *a posteriori* biomass burning emissions at $0.5° \times 0.667°$ increase in the adjoint inversion but decrease in the analytical inversion, relative to the *a priori*. In the WUS, the analytical inversions show factors of 3–5 increase of the biomass burning emissions and a ~50% reduction of the anthropogenic emissions, relative to the corresponding *a priori* (Mao et al., 2014). In contrast, both the biomass burning and anthropogenic emissions in the adjoint inversions increase by two folds (Table 1). The total *a posteriori* emissions are rather comparable (within 20–50%) between the two inversions.

Mao et al. (2014) have examined in detail the quality of the analytical inversions. The robustness of the analytical inversions and the relative consistency in the total *a posteriori* emissions from the two inversion methods therefore imply that the adjoint inversion results, at least the total emissions, are robust on the model grid scale. We will examine the robustness of the adjoint inversions further in Sect. 4.4. The large differences in the *a posteriori* anthropogenic and biomass burning emissions between the two inversion methods are largely because the inversion system has difficulty effectively distinguishing collocated biomass burning and anthropogenic emissions on model grid scales. As a result, the adjoint inversions tend to falsely impose larger anthropogenic emissions in the regions where the collocated biomass burning emissions are too low (Sects. 4.1.3 and 4.2). Jiang et al. (2011) also found that the adjoint inversion system is unable to distinguish CO emissions from collocated combustion and oxidation sources and they therefore lumped the two sectors in their inversions. The differences are also due to the large aggregation errors in the analytical inversions and the assumption of spatially uncorrelated *a priori* errors in the adjoint inversions (Sects. 3.2 and 3.4).

We further separate the anthropogenic-dominated regions to examine the ability of the adjoint inversion system to constrain collocated emissions. In the regions where anthropogenic emissions are dominant, model surface BC concentrations are in good agreement with IMPROVE observations (Mao et al., 2011) and both the *a posteriori* anthropogenic and biomass burning emissions see substantial yet still relatively small increases. For example, the *a posteriori* anthropogenic and biomass burning emissions in Washington and Oregon increase by 39 and 29%. However, in the regions where biomass burning emissions become more important but significantly underestimated, model surface BC concentrations are biased low and both the *a*

posteriori anthropogenic and biomass burning emissions increase dramatically. For example, in Montana, Idaho, and Wyoming, the *a posteriori* anthropogenic and biomass burning emissions increase by factors of 2.2 and of 2.7. In Utah, Colorado, Arizona, and New Mexico, the corresponding emissions increase by factors of 1.8 and of 1.3. In California and Nevada, the emissions increase both by a factor of 1.8.

4.4 Evaluation against observations

Model simulated surface BC concentrations with the *a posteriori* emissions show significant enhancements and largely reproduce both the synoptic variability and magnitudes of the observed surface BC concentrations, not only at individual sites (Fig. 8) but also on average at four altitude ranges (below 1, 1–2, 2–3, and above 3 km) (Fig. 9). For instance, model surface BC concentrations after the adjoint inversions capture the major fire episodes at Starkey, OR (45.2 °N, 118.5 °W, 1.26 km) and Lassen Volcanic, CA (40.5 °N, 121.6 °W, 1.73 km). The adjoint inversions at 0.5 °×0.667 ° provide better agreements with the observations than the analytical inversion results do at some sites, for example, Three Sisters, OR (44.3 °N, 122.0 °W, 0.89 km) and Pasayten, WA (48.4 °N, 119.9 °W, 1.63 km). At other sites, Jarbidge Wild, NV (41.9 °N, 115.4 °W, 1.87 km), for example, results from the analytical inversions are noticeably better. The two inversion results differ the most at 1–2 km altitudes and to a lesser degree at higher altitudes, for example, Bridger Wild, WY (43.0 °N, 109.8 °W, 2.63 km). The *a posteriori* emissions lead to an average bias reduction of ~50% in the simulated surface BC concentrations at 1–2 km altitudes (Fig. 9). Model simulated surface BC concentrations with the *a posteriori* emissions from the adjoint inversions, especially at 0.5 °×0.667 °, show substantial enhancements during major fire episodes. The enhancements are evident at all altitudes (up to 0.2 μg m^{-3} at 1–2 km and 0.1 μg m^{-3} at 2–3 km). The *a posteriori* emissions lead to large mean bias reductions (34% at 2 °×2.5 ° and 20% at 0.5 °×0.667 ° for August), as shown in Fig. 10. The frequency distributions of the bias of the 24-hour average surface BC concentrations are Gaussian (Fig. 11), as expected. The inversions reduce both the mean (by ~35% at 2 °×2.5 ° and ~15% at 0.5 °×0.667 ° for July–September) and standard deviation of the biases.

Taylor diagram and skill score (*S*) are useful measures of model accuracy. The diagram relates the centered root mean square error (RMSE), the pattern correlation (*r*) and the standard

deviation (σ) of observations and model results (Taylor, 2001). *S* (0–1) increases with increasing correlations and as the modeled variance approaches the observed variance. Fig. 12 presents the resulting diagram and skill scores of the observations and the multitude of model results. Model results with the *a posteriori* emissions are consistently in better agreement with the observations, especially using the nested model. The *a posteriori* emissions lead to higher *r* (by 11–48% on average), larger σ (by 27–122% on average), and lower centered RMSEs, thereby increasing the skill scores (by 43–221%). The *a posteriori* emissions from the adjoint inversion at 0.5 °×0.667 ° show the smallest centered RMSE and largest *r*, whereas the *a posteriori* emissions from the analytical inversion at 0.5 °×0.667 °show the largest σ and *S* values.

There are large uncertainties in the *a posteriori* emissions, as evident in the 20–30% low bias in modeled surface BC concentrations. The uncertainties are partially because of the limitations of the inversion system, in both the nature of the inverse modeling and the spatiotemporal coverage of IMPROVE observations (see Sects. 4.1.3 and 4.2). The adjoint inversion system has sufficient information to constrain the total emissions of BC, especially at the coarse resolution 2 °×2.5 °. The inversion system however has difficulty in partitioning collocated anthropogenic versus biomass burning emissions. Furthermore, comparing localized observations with coarse-resolution model results is inherently problematic (Mao et al., 2011; Fairlie et al., 2007). It is even more so because many of the IMPROVE sites are mountainous and the associated upslope flow is difficult to represent in a global model.

5. Summary and conclusions

We have applied adjoint inversions to estimate biomass burning and anthropogenic emissions of BC in the WUS for July–September 2006 by inverting the surface BC concentrations from the IMPROVE network using the GEOS-Chem chemical transport model and its adjoint. The *a posteriori* emissions of BC differed considerably between the adjoint and analytical inversions (Mao et al., 2014), especially in the partitioning of anthropogenic versus biomass burning emissions. The total was ~20–50% larger in the adjoint inversions than in the analytical inversions. Both the biomass burning and anthropogenic emissions from the adjoint inversions doubled, whereas the analytical inversions showed factors of 3–5 increases in the former and ~50%

reductions in the latter. We attributed these differences to the inability of the adjoint inversion system to effectively distinguish collocated biomass burning and anthropogenic emissions on the model grid scales. That inability resulted in excessively large anthropogenic emissions in the regions where biomass burning emissions were underestimated.

The inversions with various pseudo observations indicated that observations of surface BC concentration covering half of the model grid boxes had sufficient information to constrain the total emissions of BC on the model grid scales. IMPROVE observations of BC have sufficient information to constrain the total BC emissions at the model grid scales, especially at 2 °×2.5 °. The limitations of the adjoint inversion system, including the spatiotemporal coverage of the IMPROVE observations of BC, call for concurrent measurements of other combustion tracers (e.g., CO and carbon isotopes). Other factors may also improve the inversions, e.g., increase measurements in the source regions, or considering the spatial correlation of the *a priori* errors in the inversions.

Acknowledgements. This research was supported by NASA grant NNX09AF07G from the Atmospheric Chemistry Modeling and Analysis Program (ACMAP). The GEOS-Chem model is managed by the Atmospheric Chemistry Modeling group at Harvard University; support for the adjoint comes the Henze group at CU Boulder, which additionally recognizes support from EPA-STAR grant 83503701 (this manuscript does not reflect official EPA agency views or policies). We thank Feng Deng and Ray Nassar for helpful discussions.

References

Anenberg, S. C, Talgo, K., Arunachalam, S., Dolwick, P., Jang, C., and West, J. J.: Impacts of global, regional, and sectoral black carbon emission reductions on surface air quality and human mortality, Atmos. Chem. Phys., 11, 7253–7267, 2011.

Anenberg, S. C., Schwartz, J., Shindell, D., Amann, M., Faluvegi, G., Klimont, Z., Janssens-Maenhout, G., Pozzoli, L., Van Dingenen, R., Vignati, E., Emberson, L., Muller, N. Z., West, J. J., Williams, M., Demkine, V., Hicks, W. K., Kuylenstierna, J., Raes, F., and Ramanathan, V.: Global air quality and health co-benefits of mitigating near-term climate change through methane and black carbon emission controls, Environmental Health Perspectives, 120(6), 831–839, 2012.

Arakawa, A., and Schubert, W. H.: Interaction of a cumulus cloud ensemble with the large-scale environment, Part I, J. Atmos. Sci., 31, 674–701, 1974.

Arellano, A. F., Kasibhatla, P. S., Giglio, L., van der Werf, G. R., and Randerson, J. T.: Top-down estimates of global CO sources using MOPITT Measurements, Geophys. Res. Lett., 31, L01104, doi:10.1029/2003GL018609, 2004.

Arellano, A. F., Kasibhatla, P. S., Giglio, L., van der Werf, G. R., Randerson, J. T., and Collatz, G. J.: Time-dependent inversion estimates of global biomass-burning CO emissions using Measurement of Pollution in the Troposphere (MOPITT) measurements, J. Geophys. Res., 111, D09303, doi:10.1029/2005JD006613, 2006.

Arellano, A. F., Raeder, K., Anderson, J. L., Hess, P. G., Emmons, L. K., Edwards, D. P., Pfister, G. G., Campos, T. L., and Sachse, G. W.: Evaluating model performance of an ensemble-based chemical data assimilation system during INTEX-B field mission, Atmos. Chem. Phys., 7, 5695–5710, doi:10.5194/acp-7-5695-2007, 2007.

Bench, G.: Measurement of contemporary and fossil carbon contents of $PM_{2.5}$ aerosols: results from Turtleback Dome, Yosemite National Park, Environ. Sci. Technol., 38, 2424–2427, 2004.

Bench, G., Fallon, S., Schichtel, B., Malm, and W., McDade, C.: Relative contributions of fossil and contemporary carbon sources to $PM_{2.5}$ aerosols at nine Interagency Monitoring for Protection of Visual Environments (IMPROVE) network sites, J. Geophys. Res., 112, D10205, doi:10.1029/2006JD007708, 2007.

Bey, I., Jacob, D. J., Yantosca, R. M., Logan, J. A., Field, B. D., Fiore, A. M., Li, Q., Liu, H.-Y., Mickley, L. J., and Schultz, M. G.: Global modeling of tropospheric chemistry with assimilated meteorology: Model description and evaluation, J. Geophys. Res., 106, 23073–23095, 2001.

Bond, T. C., Streets, D. G., Yarber, K. F., Nelson, S. M., Woo, J.-H., and Klimont, Z.: A technology-based global inventory of black and organic carbon emissions from combustion, J. Geophys. Res., 109, D14203, doi:10.1029/2003JD003697, 2004.

Bond, T., and Sun, H.: Can Reducing Black Carbon Emissions Counteract Global Warming? Environ. Sci. Technol., 39, 5921–5926, 2005.

Bond, T. C., Bhardwaj, E., Dong, R., Jogani, R., Jung, S., Roden, C., Streets, D. G., and Trautmann, N. M.: Historical emissions of black and organic carbon aerosol from energy-

related combustion, 1850–2000, Global Biogeochem. Cycles, 21, GB2018, doi:10.1029/2006GB002840, 2007.

Bond, T. C., Doherty, S. J., Fahey, D. W., Forster, P. M., Berntsen, T., DeAngelo, B. J., Flanner, M. G., Ghan, S., Kärcher, B., Koch, D., Kinne, S., Kondo, Y., Quinn, P. K., Sarofim, M. C., Schultz, M. G., Schulz, M., Venkataraman, C., Zhang, H., Zhang, S., Bellouin, N., Guttikunda, S. K., Hopke, P. K., Jacobson, M. Z., Kaiser, J. W., Klimont, Z., Lohmann, U., Schwarz, J. P., Shindell, D., Storelvmo, T., Warren, S. G., and Zender, C. S.: Bounding the role of black carbon in the climate system: A scientific assessment, J. Geophys. Res., 118, 5380–5552, doi: 10.1002/jgrd.50171, 2013.

Cannon, S. H., and DeGraff, J.: The Increasing Wildfire and Post-Fire Debris-Flow Threat in Western USA, and Implications for Consequences of Climate Change, pp 177-190, Springer, Verlag Berlin Heidelberg, 2009.

Chai, T., Carmichael, G. R., Tang, Y., Sandu, A., Heckel, A., Richter, A., and Burrows, J. P.: Regional NOx emission inversion through a four-dimensional variational approach using SCIAMACHY tropospheric NO_2 column observations, Atmos. Environ.,43, 5046–5055, 2009.

Chevallier, F., Bréon, F.-M. and Rayner, P. J.: Contribution of the Orbiting Carbon Observatory to the estimation of CO_2 sources and sinks: Theoretical study in a variational data assimilation framework, J. Geophys. Res., 112, D09307, doi:10.1029/2006JD007375, 2007.

Chevallier, F., Fortems, A., Bousquet, P., Pison, I., Szopa, S., Devaux, M., and Hauglustaine, D. A.: African CO emissions between years 2000 and 2006 as estimated from MOPITT observations, Biogeosciences, 6, 103–111, 2009.

Chen, D., Wang, Y., McElroy, M. B., He, K., Yantosca, R. M., and Sager, P. L.: Regional CO pollution in China simulated by the high-resolution nested-grid GEOS-Chem model, Atmos. Chem. Phys., 9, 3825–3839, 2009.

Chin, M., Ginoux, P., Kinne, S., Torres, O., Holben, B. N., Duncan, B. N., Martin, R. V., Logan, J. A., Higurashi, A., and Nakajima, T.: Tropospheric aerosol optical thickness from the GOCART model and comparisons with satellite and sun photometer measurements, J. Atmos. Sci., 59, 461–483, 2002.

Chow, J. C., Watson, J. G., Pritchett, L. C., Pierson, W. R., Frazier, C. A., and Purcell, R. G.: The DRI thermal/optical reflectance carbon analysis system: Description, evaluation, and applications in U.S. air quality studies, Atmos. Environ., 27A(8), 1185–1201, 1993.

Chow, J. C., Watson, J. G., Chen, L. W. A., Arnott, W. P., and Moosmuller, H.: Equivalence of elemental carbon by thermal/optical reflectance and transmittance with different temperature protocols, Environ. Sci. Technol., 38, 4414–4422, 2004.

Cooke, W. F., Liousse, C., Cachier, H., and Feichter, J.: Construction of a 1 °×1 ° fossil fuel emission data set for carbonaceous aerosol and implementation and radiative impact in the ECHAM4 model, J. Geophys. Res., 104(D18), 22137–22162, 1999.

Dubovik, O., Lapyonok, T., Kaufman, Y. J., Chin, M., Ginoux, P., Kahn, R. A., and Sinyuk, A.: Retrieving global aerosol sources from satellites using inverse modeling, Atmos. Chem. Phys., 8, 209–250, 2008.

Fairlie, T. D., Jacob, D. J. and Park, R. J.: The impact of transpacific transport of mineral dust in the United States, Atmos. Environ., 41, 1251–1266, 2007.

Flanner, M. G., Zender, C. S., Randerson, J. T., and Rasch, P. J.: Present-day climate forcing and response from black carbon in snow, J. Geophys. Res., 112, D11202, doi:10.1029/2006JD008003, 2007.

Flanner, M. G., Zender, C. S., Hess, P. G., Mahowald, N. M., Painter, T. H., Ramanathan, V. and Rasch, P. J.: Springtime warming and reduced snow cover from carbonaceous particles, Atmos. Chem. Phys., 9, 2481–2497, 2009.

Fu, T. M., Cao, J. J., Zhang, X. Y., Lee, S. C., Zhang, Q., Han, Y. M., Qu, W. J., Han, Z., Zhang, R., Wang, Y. X., Chen, D., and Henze, D. K.: Carbonaceous aerosols in China: top-down constraints on primary sources and estimation of secondary contribution, Atmospheric Chemistry and Physics, 12(5), 2725–2746, 2012.

Fuglestvedt, J. S., Shine, K. P., Bernsten, T., Cook, J., Lee, D. S., Stenke, A., Skeie, R. B., Velders, G. J. M., and Waitz, I. A.: Transport impacts on atmosphere and climate: Metrics, Atmos. Environ., 44, 4648–4677, 2010.

Giglio, L., van der Werf, G. R., Randerson, J. T., Collatz, G. J., and Kasibhatla, P.: Global estimation of burned area using MODIS active fire observations, Atmos. Chem. Phys., 6, 957–974, 2006.

Giglio, L., Randerson, J. T., van der Werf, G. R., Kasibhatla, P. S., Collatz, G. J., Morton, D. C., and DeFries, R. S.: Assessing variability and long-term trends in burned area by merging multiple satellite fire products, Biogeosciences, 7, 1171–1186, 2010.

Gleckler, P. J., Taylor, K. E., and Doutriaux, C.: Performance metrics for climate models, J. Geophys. Res., 113, D06104, doi:10.1029/2007JD008972, 2008.

Gloor, M., Fan, S.-M., Pacala, S. W., Sarmiento, J. L., and Ramonet, M.: A model-based evaluation of inversions of atmospheric transport, using annual mean mixing ratios, as a tool to monitor fluxes of nonreactive trace substances like CO_2 on a continental scale, J. Geophys. Res., 104, 14245–14260, 1999.

Hack, J. J.: Parameterization of moist convection in the NCAR community climate model (CCM2), J. Geophys. Res., 99, 5551–5568, doi:10.1029/93JD03478, 1994.

Hakami, A., Henze, D. K., Seinfeld, J. H., Chai, T., Tang, Y., Carmichael, G. R., and Sandu, A.: Adjoint inverse modeling of black carbon during the Asian Pacific Regional Aerosol Characterization Experiment, J. Geophys. Res., 110(D14), D14301, doi:10.1029/2004JD005671, 2005.

Han, S., Kondo, Y., Oshima, N., Takegawa, N., Miyazaki, Y., Hu, M., Lin, P., Deng, Z., Zhao, Y., Sugimoto, N., and Wu, Y.: Temporal variations of elemental carbon in Beijing, J. Geophys. Res., 114(D23), D23202, doi:10.1029/2009jd012027, 2009.

Hansen, J., and Nazarenko, L.: Soot climate forcing via snow and ice albedos, PNAS, 101(2), 423–428, 2004.

Heal, M. R.: The application of carbon-14 analyses to the source apportionment of atmospheric carbonaceous particulate matter: a review, Anal. Bioanal. Chem., 406, 81–98, DOI 10.1007/s00216-013-7404-1, 2014.

Heald, C. L., Jacob, D. J., Jones, D. B. A., Palmer, P. I., Logan, J. A., Streets, D. G., Sachse, G. W., Gille, J. C., Hoffman, R. N., and Nehrkorn, T.: Comparative inverse analysis of satellite (MOPITT) and aircraft (TRACE-P) observations to estimate Asian sources of carbon monoxide, J. Geophys. Res., 109, D15S04, doi:10.1029/2004JD005185, 2004.

Hein, R., Crutzen, P. J., and Heimann, M.: An inverse modeling approach to investigate the global atmospheric methane cycle, Global Biogeochemical Cycles, 11(1): 43–76, 1997.

Henze, D. K., Hakami, A., and Seinfeld, J. H.: Development of the adjoint of GEOS-Chem, Atmos. Chem. Phys., 7, 2413–2433, doi:10.5194/acp-7-2413-2007, 2007.

Henze, D. K., Seinfeld, J. H., and Shindell, D. T.: Inverse modeling and mapping US air quality influences of inorganic PM2.5 precursor emissions using the adjoint of GEOS-Chem, Atmos. Chem. Phys., 9, 5877–5903, doi:10.5194/acp-9-5877-2009, 2009.

Horvath, H.: Atmospheric light absorption–A review, Atmos. Environ., 27, 293–317, 1993.

Intergovernmental Panel on Climate Change (IPCC), The Physical Science Basis, edited by: Solomon, S., Qin, D., Manning, M., Chen, Z., Marquis, M., Averyt, K. B., Tignor M., and Miller, H. L.: Contribution of Working Group I to the Fourth Assessment Report of the Intergovernmental Panel on Climate Change, Cambridge Univ. Press, Cambridge, UK, 2007.

Jacob, D. J.: Lectures on inverse modeling, Harvard University, Cambridge, USA, January 2007, 25pp.

Huebert, B. J., Bates, T., Russell, P. B., Shi, G., Kim, Y. J., Kawamura, K., Carmichael, G., and Nakajima, T.: An overview of ACE-Asia: Strategies for quantifying the relationships between Asian aerosols and their climatic impacts, J. Geophys. Res., 108(D23), 8633, doi:10.1029/2003JD003550, 2003.

Jacobson, M.Z.: Strong radiative heating due to the mixing state of black carbon in atmospheric aerosols, Nature, 409, 695–697, 2001.

Jacobson, M. Z.: Control of fossil-fuel particulate black carbon and organic matter, possibly the most effective method of slowing global warming, J. Geophys. Res., 107(D19), 4410, doi:10.1029/2001JD001376, 2002.

Jacobson, M. Z.: Climate response of fossil fuel and biofuel soot, accounting for soot's feedback to snow and sea ice albedo and emissivity, J. Geophys. Res., 109, D21201, doi:10.1029/2004JD004945, 2004.

Jacobson, M. Z.: Short-term effects of controlling fossil-fuel soot, biofuel soot and gases, and methane on climate, Arctic ice, and air pollution health, J. Geophys. Res., 115, D14209, doi.10.1029/2009JD013795, 2010.

Jiang, Z., Jones, D. B. A., Kopacz, M., Liu, J., Henze, D. K., and Heald, C.: Quantifying the impact of model errors on top-down estimates of carbon monoxide emissions using satellite observations, J. Geophys. Res., 116, D15306, doi:10.1029/2010JD015282, 2011.

Jiang, Z., Jones, D. B. A., Worden, H. M., Deeter, M. N., Henze, D. K., Worden, J., Bowman, K. W., Brenninkmeijer, C. A. M., and Schuck, T. J.: Impact of model errors in convective transport on CO source estimates inferred from MOPITT CO retrievals, J. Geophys. Res. Atmos., 118, 2073–2083, doi:10.1002/jgrd.50216, 2013.

Jiang, Z., Jones, D. B. A, Worden, J., Worden, H. M., Henze, D. K., and Wang, Y.: Regional data assimilation of multi-spectral MOPITT observations of CO over North America, Atmos. Chem.

Phys. Discuss., 15, 5327-5358, 2015a.

Jiang, Z., Jones, D. B. A, Worden, H. M., and Henze, D. K.: Sensitivity of top-down CO source estimates to the modeled vertical structure in atmospheric CO, Atmos. Chem. Phys., 15, 1521-1537, 2015b.

Jin, Y., Randerson, J. T., Faivre, N., Capps, S., Hall, A., and Goulden, M. L.: Contrasting controls on wildland fires in Southern California during periods with and without Santa Ana winds, Journal of Geophysical Research: Biogeosciences, 119(3), 432–450, 2014.

Jones, D. B. A., Bowman, K. W., Logan, J. A., Heald, C. L., Liu, J., Luo, M., Worden, J., and Drummond, J.: The zonal structure of tropical O_3 and CO as observed by the Tropospheric Emission Spectrometer in November 2004–Part 1: Inverse modeling of CO emissions, Atmos. Chem. Phys., 9, 3547–3562, doi:10.5194/acp-9-3547-2009, 2009.

Kopacz, M., Jacob, D. J., Henze, D. K., Heald, C. L., Streets, D. G., and Zhang, Q.: Comparison of adjoint and analytical bayesian inversion methods for constraining Asian sources of carbon monoxide using satellite (MOPITT) measurements of CO columns, J. Geophys. Res., 114, D04305, doi:10.1029/2007JD009264, 2009.

Kopacz, M., Jacob, D. J., Fisher, J. A., Logan, J. A., Zhang, L., Megretskaia, I. A., Yantosca, R. M., Singh, K., Henze, D. K., Burrows, J. P., Buchwitz, M., Khlystova, I., McMillan, W. W., Gille, J. C., Edwards, D. P., Eldering, A., Thouret, V., and Nedelec, P.: Global estimates of CO sources with high resolution by adjoint inversion of multiple satellite datasets (MOPITT, AIRS, SCIAMACHY, TES), Atmos. Chem. Phys., 10, 855–876, doi:10.5194/acp-10-855-2010, 2010.

Kopacz, M., Mauzerall, D. L., Wang, J., Leibensperger, E. M., Henze, D. K., and Singh, K.: Origin and radiative forcing of black carbon transported to the Himalayas and Tibetan Plateau, Atmos. Chem. Phys., 11, 2837–2852, doi:10.5194/acp-11-2837-2011, 2011.

Kopp, R. E. and Mauzerall, D. L.: Assessing the climatic benefits of black carbon mitigation, P. Natl. Acad. Sci., 26, 11703 11708, 2010.

Korontzi, S., McCarty, J., Loboda, T., Kumar, S., and Justice, C.: Global distribution of agricultural fires in croplands from 3 years of Moderate Resolution Imaging Spectroradiometer (MODIS) data, Global Biogeochem. Cy., 20, GB2021, doi:10.1029/2005GB002529, 2006.

Langmann, B., Duncan, B., Textor, C., Trentmann, J., van der Werf, G. R.: Vegetation fire emissions and their impact on air pollution and climate, Atmos. Environ., 43, 107–116, 2009.

Lee, C., Martin, R. V., van Donkelaar, A., Lee, H., Dickerson, R. R., Hains, J. C., Krotkov, N., Richter, A., Vinnikov, K., and Schwab, J. J.: SO_2 emissions and lifetimes: Estimates from inverse modeling using in situ and global, space-based (SCIAMACHY and OMI) observations, J. Geophys. Res., 116, D06304, doi:10.1029/2010JD014758, 2011.

Levy II, H., Schwarzkopf, M. D., Horowitz, L., Ramaswamy, V., and Findell, K. L.: Strong sensitivity of late 21st century climate to projected changes in short-lived air pollutants, J. Geophys. Res., 113, D06102, doi:10.1029/2007JD009176, 2008.

Lewis, C. W., Klouda, G. A., and Ellenson, W. D.: Radiocarbon measurement of the biogenic contribution to summertime $PM_{2.5}$ ambient aerosol in Nashville, TN, Atmos. Environ., 38, 6053–6061, 2004.

Lin, J. T., McElroy, M. B., and Boersma, K. F.: Constraint of anthropogenic NOx emissions in China from different sectors: A new methodology using multiple satellite retrievals, Atmos. Chem. Phys., 10, 63–78, doi:10.5194/acp-10-63-2010.

Lin, S.-J., and Rood, R. B.: Multidimensional flux-form semi-Lagrangian transport schemes, Mon. Weather Rev., 124, 2046–2070, 1996.

Liu, D. C., and Nocedal, J.: On the limited memory BFGS method for large scale optimization, Math. Program., 45, 503–528, doi:10.1007/BF01589116, 1989.

Liu, H., Jacob, D. J., Bey, I., and Yantosca, R. M.: Constraints from ^{210}Pb and ^{7}Be on wet deposition and transport in a global three-dimensional chemical tracer model driven by assimilated meteorological fields, J. Geophys. Res., 106, 12109-12128, 2001.

Martin, R. V., Jacob, D. J., Chance, K., Kurosu, T. P., Palmer, P. I., and Evans, M. J.: Global inventory of nitrogen oxide emissions constrained by space-based observations of NO2 columns, J. Geophys. Res., 108(D17), 4537, doi:10.1029/2003JD003453, 2003.

Martin, R. V., Sioris, C. E., Chance, K., Ryerson, T. B., Bertram, T. H., Wooldridge, P. J., Cohen, R. C., Neuman, J. A., Swanson, A., and Flocke, F. M.: Evaluation of space-based constraints on global nitrogen oxide emissions with regional aircraft measurements over and downwind of eastern North America, J. Geophys. Res., 111, D15308, doi:10.1029/2005JD006680, 2006.

Mao, Y. H., Li, Q. B., Zhang, L., Chen, Y., Randerson, J. T., Chen, D., and Liou, K.-N.: Biomass burning contribution to black carbon in theWestern United States Mountain Ranges, Atmos. Chem. Phys., 11, 11253–11266, 2011.

Mao, Y. H., Li, Q. B., Randerson, J. T., Chen, D., Zhang, L., Hao, W.-M., and Liou, K.-N.: Top-down estimates of biomass burning emissions of black carbon in the Western United States, Atmos. Chem. Phys., 14, 7195–7211, 2014.

Malm, W. C., Sisler, J. F., Huffman, D., Eldred, R. A., and Cahill, T. A.: Spatial and seasonal trends in particle concentration and optical extinction in the United States, J. Geophys. Res., 99, 1347–1370, 1994.

Meirink, J. F., Bergamaschi, P., and Krol, M. C.: Four-dimensional variational data assimilation for inverse modelling of atmospheric methane emissions: Method and comparison with synthesis inversion, Atmospheric Chemistry and Physics, 8(21), 6341–6353, 2008.

Melillo, J. M., Richmond, T.C., and Yohe, G. W.: Climate Change Impacts in the United States: The Third National Climate Assessment, U.S. Global Change Research Program, 841 pp, doi:10.7930/J0Z31WJ2, 2014.

McCarty, J. L., Korontzi, S., Justice, C. O., and Loboda, T.: The spatial and temporal distribution of crop residue burning in the contiguous United States, Sci. Total Environ., 407(21), 5701–5712, doi:10.1016/j.scitotenv.2009.07.009, 2009.

McMurry, P. H., Shepherd, M. F., and Vickery, J. S.: Particulate Matter Science for Policy Makers: A NARSTO Assessment, Cambridge University Press, New York, NY, 2004.

Moorthi, S., and Suarez, M. J.: Relaxed Arakawa-Schubert: A parameterization of moist convection for general circulation models, Mon. Wea. Rev., 120, 978–1002, 1992.

Müller, J.-F., and Stavrakou, T.: Inversion of CO and NO_x emissions using the adjoint of the IMAGES model, Atmos. Chem. Phys., 5, 1157–1186, 2005.

Painter, T. H., Flanner, M. G., Kaser, G., Marzeion, B., VanCuren, R. A., and Abdalati, W.: End of the Little Ice Age in the Alps forced by industrial black carbon, Proceedings of the National Academy of Sciences, 110(38), 15216–15221, 2013.

Park, R. J., Jacob, D. J., Chin, M., and Martin, R. V.: Sources of carbonaceous aerosols over the United States and implications for natural visibility, J. Geophys. Res., 108, D124355, doi:10.1029/2002JD003190, 2003.

Parrington, M., Palmer, P. I., Henze, D. K., Tarasick, D. W., Hyer, E. J., Owen, R. C., Clerbaux, C., Bowman, K. W., Deeter, M. N., Barratt, E. M., Coheur, P.-F., Hurtmans, D., George, M., and Worden, J. R.: The influence of boreal biomass burning emissions on the distribution of

tropospheric ozone over North America and the North Atlantic during 2010, Atmos. Chem. Phys., 12, 2077–2098, 2012.

Paulot, F., Jacob, D. J., Pinder, R. W., Bash, J. O., Travis, K., and Henze, D. K.: Ammonia emissions in the United States, European Union, and China derived by high-resolution inversion of ammonium wet deposition data: Interpretation with a new agricultural emissions inventory (MASAGE_NH_3), J. Geophys. Res. Atmos., 119, 4343–4364, doi:10.1002/2013JD021130, 2014.

Peterson, D. L., and Marcinkowski, K. W.: Recent Changes in Climate and Forest Ecosystems, Climate Change and United States Forests, Springer, Dordrecht, the Netherlands, 57, 3–11, 2014.

Pickett-Heaps, C. A., Rayner, P. J., Law, R. M., Ciais, P., Patra, P. K., Bousquet, P., Peylin, P., Maksyutov, S., Marshall, J., Rödenbeck, C., Langenfelds, R. L., Steele, L. P., Francey, R. J., Tans, P., and Sweeney, C.: Atmospheric CO_2 inversion validation using vertical profile measurements: Analysis of four independent inversion models, J. Geophys. Res., 116, D12305, doi:10.1029/2010JD014887, 2011.

Qian, Y., Gustafson Jr., W. I., Leung, L. R., and Ghan, S. J.: Effects of soot-induced snow albedo change on snowpack and hydrological cycle in western United States based on Weather Research and Forecasting chemistry and regional climate simulations, J. Geophys. Res., 114, D03108, doi:10.1029/2008JD011039, 2009.

Ramana, M. V., Ramanathan, V., Feng, Y., Yoon, S.-C., Kim, S.-W., Carmichael, G. R., and Schauer, J. J.: Warming influenced by the ratio of black carbon to sulphate and the black carbon source, Nature Geoscience, 3, 542–545, 2010.

Ramanathan, V. and Carmichael, G.: Global and regional climate changes due to black carbon, Nature Geoscience, 1, 221–227, 2008.

Randerson, J. T., van der Werf, G. R., Giglio, L., Collatz, G. J., and Kasibhatla, P. S.: Global Fire Emissions Database, Version 2 (GFEDv2) (http://daac.ornl.gov/ (last acess: 2013)), Oak Ridge National Laboratory Distributed Active Archive Center, Oak Ridge, Tennessee, U.S.A., 2007.

Randerson, J. T., Chen, Y., van der Werf, G.R., Rogers, B. M., and Morton, D. C.: Global burned area and biomass burning emissions from small fires, J. Geophys. Res., 117, G04012, doi:10.1029/2012JG002128, 2012.

Reche, C., Querol, X., Alastuey, A., Viana, M., Pey, J., Moreno, T., Rodríguez, S., González, Y., Fernández-Camacho, R., de la Rosa, J., Dall'Osto, M., Prévôt, A. S. H., Hueglin, C., Harrison, R. M., and Quincey, P.: New considerations for PM, Black Carbon and particle number concentration for air quality monitoring across different European cities, Atmos. Chem. Phys., 11, 6207–6227, doi:10.5194/acp-11-6207-2011, 2011.

Reddy, M. S. and Boucher, O.: Climate impact of black carbon emitted from energy consumption in the world's regions, Geophys. Res. Lett., 34, L11802, doi:10.1029/2006GL028904, 2007.

Rodgers, C. D.: Inverse Methods for Atmospheric Sounding: Theory and Practice, World Sci., Singapore, 2000.

Roy, D. P., and Boschetti, L.: Southern Africa validation of the MODIS, L3JRC, and GlobCarbon burned-area products, IEEE Trans. Geosci. Remote Sens., 47(4), 1032–1044, doi:10.1109/TGRS.2008.2009000, 2009.

Schichtel, B. A., Malm, W. C., Bench, G., Fallon, S., McDade, C. E., Chow, J. C., and Watson, J. G. : Fossil and contemporary fine particulate carbon fractions at 12 rural and urban sites in the United States, J. Geophys. Res., VOL. 113, D02311, doi:10.1029/2007JD008605, 2008.

Seinfeld, J. H., Carmichael, G. R., Arimoto, R., Conant, W. C., Brechtel, F. J., Bates, T. S., Cahill, T. A., Clarke, A. D., Doherty, S. J., Flatau, P. J., Huebert, B. J., Kim, J., Markowicz, K. M., Quinn, P. K., Russell, L. M., Russell, P. B., Shimizu, A., Shinozuka, Y., Song, C. H., Tang, Y., Uno, I., Vogelmann, A. M., Weber, R. J., Woo, J.-H., and Zhang, X. Y.: ACE-ASIA-Regional climatic and atmospheric chemical effects of Asian dust and pollution, Bull. Am. Meteorol. Soc., 85 (3), 367–380, ISSN 0003-0007, 2004.

Shindell, D. T., Levy, H. II, Schwarzkopf, M. D., Horowitz, L. W., Lamarque, J.-F., and Faluvegi, G.: Multimodel projections of climate change from short-lived emissions due to human activities, J. Geophys. Res., 113, D11109, doi:10.1029/2007JD009152, 2008.

Shindell, D, Kuylenstierna, J. C. I., Vignati, E., van Dingenen, R., Amann, M., Klimont, Z., Anenberg, S. C., Muller, N., Janssens-Maenhout, G., Raes, F., Schwartz, J., Faluvegi, G., Pozzoli, L., Kupiainen, K., Höglund-Isaksson, L., Lisa Emberson, L., Streets, D., Ramanathan, V., Hicks, K., Kim Oanh, N. T., George Milly, G., Martin Williams, M., Demkine, V., and Fowler, D.: Simultaneously mitigating near-term climate change and improving human health and food security, Sciences, 335(13), 183–189, 2012.

Smith, K. R., Jerrett, M., Anderson, H. R., Burnett, R. T., Stone, V., Derwent, R., Atkinson, R. W., Cohen, A., Shonkoff, S. B., Krewski, D., Pope III, C. A. , Thun, M. J., and Thurston, G.: Public health benefits of strategies to reduce greenhouse-gas emissions: health implications of short-lived greenhouse pollutants, Lancet, 374, 2091–2103, 2009.

Spackman, J. R., Schwarz, J. P., Gao, R. S., Watts, L. A., Thomson, D. S., Fahey, D. W., Holloway, J. S., de Gouw, J. A., Trainer, M., and Ryerson, T. B.: Empirical correlations between black carbon aerosol and carbon monoxide in the lower and middle troposphere, Geophys. Res. Lett., 35(19), L19816, doi:10.1029/2008GL035237, 2008.

Stavrakou, T., and Müller, J.-F.: Grid-based versus big region approach for inverting CO emissions using Measurement of Pollution in the Troposphere (MOPITT) data, J. Geophys. Res., 111, D15304, doi:10.1029/2005JD006896, 2006.

Subramanian, R., Kok, G. L., Baumgardner, D., Clarke, A., Shinozuka, Y., Campos, T. L., Heizer, C. G., Stephens, B. B., de Foy, B., Voss, P. B., and Zaveri, R. A.: Black carbon over Mexico: the effect of atmospheric transport on mixing state, mass absorption cross-section, and BC/CO ratios, Atmos. Chem. Phys., 10, 219–237, doi:10.5194/acp-10-219-2010, 2010.

Szidat, S., Jenk, T. M., Synal, H.-A., Kalberer, M., Wacker, L., Hajdas, I., Kasper-Giebl, A., and Baltensperger, U.: Contributions of fossil fuel, biomass-burning, and biogenic emissions to carbonaceous aerosols in Zurich as traced by ^{14}C, J. Geophys. Res., 111, D07206, doi:10.1029/2005JD006590, 2006.

Taylor, K. E.: Summarizing multiple aspects of model performance in a single diagram, J. Geophys. Res., 106(D7), 7183–7192, 2001.

van der Werf, G. R., Randerson, J. T., Giglio, L., Collatz, G. J., Kasibhatla, P. S. and Arellano Jr., A. F.: Interannual variability in global biomass burning emission from 1997 to 2004, Atmos. Chem. Phys., 6, 3423–3441, 2006.

van der Werf, G. R., Randerson, J. T., Giglio, L., Collatz, G. J., Mu, M., Kasibhatla, P. S., Morton, D. C., DeFries, R. S., Jin, Y., and van Leeuwen, T. T.: Global fire emissions and the contribution of deforestation, savanna, forest, agricultural, and peat fires (1997–2009), Atmos. Chem. Phys., 10, 11707–11735, doi:10.5194/acp-10-11707-2010, 2010.

Vano, J. A., Udall, B., Cayan, D. R., Overpeck, J. T., Brekke, L. D., Das, T., and Lettenmaier, D. P.: Understanding uncertainties in future Colorado River streamflow, Bulletin of the American Meteorological Society, 95, 59–78, doi:http://dx.doi.org/10.1175/BAMS-D-12-00228.1, 2013.

Walcek, C. J., Brost, R. A., and Chang, J. S.: SO2, sulfate and HNO_3 deposition velocities computed using regional landuse and meteorological data, Atmos. Environ., 20, 949-964, 1986.

Walker, T., Jones, D. B. A., Parrington, M., Henze, D. K., Murray, L. T., Bottenheim, J. W., Anlauf, K., Worden, J. R., Bowman, K. W., Shim, C., Singh, K., Kopacz, M., Tarasick, D. W., Davies, J., von der Gathen, P., and Carouge, C. C.: Impacts of midlatitude precursor emissions and local photochemistry on ozone abundances in the Arctic, J. Geophys. Res., 117, D01305 doi:10.1029/2011JD016370, 2012.

Wang, J., Xu, X., Henze, D. K., Zeng, J., Ji, Q., Tsay, S.-C., and Huang, J.:Top-down estimate of dust emissions through integration of MODIS and MISR aerosol retrievals with the GEOS-Chem adjoint model, Geophys. Res. Lett., 39, L08802, doi:10.1029/2012GL051136, 2012.

Wang, Q., Jacob, D. J., Fisher, J. A., Mao, J., Leibensperger, E. M., Carouge, C. C., Le Sager, P., Kondo, Y., Jimenez, J. L., Cubison, M. J., and Doherty, S. J.: Sources of carbonaceous aerosols and deposited black carbon in the Arctic in winter-spring: implications for radiative forcing, Atmos. Chem. Phys., 11, 12453–12473, doi:10.5194/acp-11-12453-2011, 2011.

Wang, X., Wang, Y., Hao, J., Kondo, Y., Irwin, M., Munger, J. W., and Zhao, Y.: Top-down estimate of China's black carbon emissions using surface observations: Sensitivity to observation representativeness and transport model error, J. Geophys. Res. Atmos., 118, 5781–5795, doi:10.1002/jgrd.50397, 2013.

Wang, Y., McElroy, M. B., Jacob, D., and Yantosca, R. M.: A nested grid formulation for chemical transport over Asia: applications to CO, J. Geophys. Res., 109, D22307, doi:10.1029/2004JD005237, 2004.

Wecht, K. J., Jacob, D. J., Wofsy, S. C., Kort, E. A., Worden, J. R., Kulawik, S. S., Henze, D. K., Kopacz, M., and Payne, V. H.: Validation of TES methane with HIPPO aircraft observations: implications for inverse modeling of methane sources, Atmos. Chem. Phys., 12, 1823–1832, doi:10.5194/acp-12-1823-2012, 2012.

Westerling, A. L., Hidalgo, H. G., Cayan, D. R., and Swetnam, T. W.: Warming and earlier spring increase western U.S. forest fire activity, Science, 313, 940–943, DOI: 10.1126/science.1128834, 2006.

Xu, B., Cao, J., Hansen, J., Yao, T., Joswia, D. R., Wang, N., Wu, G., Wang, M., Zhao, H., Wei Yang, W., Liu, X., and He, J.: Black soot and the survival of Tibetan glaciers, Proceedings of the National Academy of Sciences, 106(52), 22114–22118, 2009.

Xu, X., Wang, J., Henze, D. K., Qu, W., and Kopacz, M.: Constraints on Aerosol Sources Using GEOS-Chem Adjoint and MODIS Radiances, and Evaluation with Multi-sensor (OMI, MISR) data, J. Geophys. Res., 118, 6396–6413, DOI: 10.1002/jgrd.50515, 2013.

Yumimoto, K., Uno, I., Sugimoto, N., Shimizu, A., Liu, Z., and Winker, D. M.: Adjoint inversion modeling of Asian dust emission using lidar observations, Atmos. Chem. Phys., 8, 2869–2884, 2008.

Zhang, L., Jacob, D. J., Kopacz, M., Henze, D. K., Singh, K., and Jaffe, D. A.: Intercontinental source attribution of ozone pollution at western us sites using an adjoint method, Geophys. Res. Lett., 36, L11810, doi:10.1029/2009gl037950, 2009.

Zhang, L., Jacob, D. J., Downey, N. V., Wood, D. A., Blewitt, D., Carouge, C. C., van Donkelaar, A., Jones, D. B. A., Murray, L. T., and Wang, Y.: Improved estimate of the policy relevant background ozone in the United States using the GEOS-Chem global model with 1/2 °×2/3 ° horizontal resolution over North America, Atmos. Environ., 45, 6769–6776, doi:10.1016/j.atmosenv.2011.07.054, 2011.

Zhang, Y., Jaegl é, L., van Donkelaar, A., Martin, R. V., Holmes, C. D., Amos, H. M., Wang, Q., Talbot, R., Artz, R., Brooks, S., Luke, W., Holsen, T. M., Felton, D., Miller, E. K., Perry, K. D., Schmeltz, D., Steffen, A., Tordon, R., Weiss-Penzias, P., and Zsolway, R.: Nested-grid simulation of mercury over North America, Atmos. Chem. Phys., 12, 6095–6111, doi:10.5194/acp- 12-6095-2012, 2012.

Zhu, L., Henze, D. K., Cady-Pereira, K. E., Shephard, M. W., Luo, M., Pinder, R. W., Bash, J. O., and Jeong, G.-R.: Constraining U.S. ammonia emissions using TES remote sensing observations and the GEOS-Chem adjoint model, J. Geophys. Res. Atmos., 118, 3355–3368, doi:10.1002/jgrd.50166, 2013.

Zwally, H. J., Abdalati, W., Herring, T., Larson, K., Saba, J., and Steffen, K.: Surface melt-induced acceleration of Greenland ice-sheet flow, Science, 297, 218–222, 2002.

Zyrichidou, I., Koukouli, M. E., Balis, D., Markakis, K., Kioutsioukis, I., Poupkou, A., Melas, D., Boersma, K. F., and van Roozendael, M.: Compilation of a NO_x Emission Inventory for the Balkan Region Using Satellite Tropospheric NO_2 Columns, Advances in Meteorology, Climatology and Atmospheric Physics, 1265–1271, 2013.

Tables and Figures

Table 1. Monthly biomass burning and anthropogenic emissions of BC (unit: Gg) in the WUS for August 2006.

Table 2. Monthly anthropogenic and biomass burning emissions of BC (unit: Gg) in the WUS from the adjoint inversions for August 2006 using pseudo observations.

Fig. 1. IMPROVE sites (data available at http://vista.cira.colostate.edu/improve/; solid circles) in the Western United States (WUS). We use all the 69 sites in the standard inversion Case 1 (Table 1). Small 56 solid circles represent the sites used in the inversion Case 6 (Table 1). Also shown are terrain heights (color contours).

Fig. 2. Emissions of BC in the WUS for August 2006: (top two rows) biomass burning, (middle two rows) anthropogenic, and (bottom two rows) total emissions. First column: the *a priori*; second column: the optimized inventory; third column: differences between the *a posteriori* and *a priori*; fourth column: scaling factors. For the purpose of clarity, biomass burning emissions are multiplied by 2 in the figures. Retrieval results are from the standard adjoint (Case 1, Table 1) and analytical (Mao et al., 2014) inversions at 2 °×2.5 °. We assume for inversions uncertainties of 500, 50, and 30% for biomass burning BC emissions, anthropogenic BC emissions, and total observation error.

Fig. 3. Normalized sensitivities of the cost function with respect to the BC emissions (left: biomass burning BC; middle: anthropogenic BC; right: total emissions of BC) before and after the inversions at 2 °×2.5 ° (Case 1, Table 1) and 0.5 °×0.667 ° (Case 9, same as Case 1, except at 0.5 °×0.667 °) for August 2006. For the purpose of clarity, sensitivities of the cost function to biomass burning emissions are multiplied by 10 in the figures.

Fig. 4. Emissions of BC in the WUS for August 2006: (top panels) biomass burning, (middle panels) anthropogenic, and (bottom panels) total emissions. Results are from Case 6 (Table 1): (left column) the optimized inventory, (middle column) *a posteriori* - *a priori*, and (right column) the scaling factors. Case 6 is same as Case1, except with only 56 sites used in the inversion. For the purpose of clarity, biomass burning emissions are multiplied by 2 in the figures.

Fig. 5. Monthly anthropogenic and biomass burning emissions of BC in each 2 °×2.5 ° grid box for August 2006 (unit: kg). Solid line is 1:1 and dashed lines are 1:10 (or 10:1).

Fig. 6. Emissions of BC: Case 8 minus Case 1 (Table 1) at 2 °×2.5 ° for August 2006. Case 8 is same as Case 1, except with the *a priori* biomass burning emissions uniformly increased by 2.5 Mg in every model grid box.

Fig. 7. Same as **Fig. 2**, but at 0.5 °×0.667 ° (Case 9, same as Case 1, except at 0.5 °×0.667 °).

Fig. 8. Observed (red line) and GEOS-Chem simulated 24-hour average surface BC concentrations (μg m^{-3}) at six IMPROVE sites for July-September 2006. Results are for 2 °×2.5 ° (solid) and 0.5 °×0.667 ° (dotted line) with the *a priori* (black line) or *a posteriori* emissions from the analytical (blue line) or adjoint (green line) inversions.

Fig. 9. Observed (red line) and GEOS-Chem simulated 24-hour average surface BC concentrations (μg m^{-3}) for July-September 2006, averaged for the IMPROVE sites (**Fig. 1**) in altitudes below 1 km, 1–2 km, 2–3 km, and above 3 km (3 sites). Results are for 2 °×2.5 ° (solid line) and 0.5 °×0.667 ° (dotted line) with the *a priori* (black line) or *a posteriori* emissions from the analytical (blue line) or adjoint (green line) inversions.

Fig. 10. Differences between GEOS-Chem simulated and observed 24-hour average surface BC concentrations at the 69 IMPROVE sites (**Fig. 1**) for August 2006. Model results are from the adjoint inversions at 2 °×2.5 ° (Case 1, Table 1) and 0.5 °×0.667 ° (Case 9, same as Case 1, except at 0.5 °×0.667 °) with the *a priori* or *a posteriori* emissions.

Fig. 11. Frequency distribution of the bias of GEOS-Chem simulated 24-hour average surface BC concentrations for July-September 2006. Results are for 2 °×2.5 ° and 0.5 °×0.667 ° with the *a priori* or *a posteriori* emissions from the analytical or adjoint inversions. Also shown are the mean, median, standard deviation, and fitted Gaussian distribution.

Fig. 12. Taylor diagram and Taylor scores for GEOS-Chem simulations of BC for July-September 2006 at 2 °×2.5 ° (solid circle) and 0.5 °×0.667 ° (open circle) with the *a priori* (red circle) or *a posteriori* emissions from the analytical (blue circle) or adjoint (green circle) inversions. Values are averages for the 69 IMPROVE sites (**Fig. 1**).

Fig. S1. Sensitivities of surface BC mass to the scaling factors of BC emissions as computed using GEOS-Chem adjoint and the finite difference approximation (Eq. 1, unit: kg / grid box). Results are from 1-week simulations for biomass burning (top panel) and anthropogenic emissions (bottom panel) for August 2006. Solid lines are regression lines.

Fig. S2. (top) Normalized *a posteriori* cost function $J(\boldsymbol{X}_n)/J(\boldsymbol{X}_0)$ as a function of the regularization parameter γ_r (Eq. 3) for August 2006. (bottom) Reduction in the normalized cost function $J(\boldsymbol{X}_i)/J(\boldsymbol{X}_0)$ at 2 °×2.5 ° and 0.5 °×0.667 ° for August 2006.

Table 1. Monthly biomass burning and anthropogenic emissions of BC (unit: Gg) in the WUS for August 2006.

			Inversion configurations						Emissions[a] (Gg (10^9 g))					
			Model Resolution	Site num.	S_aBB (%)	S_aAnth (%)	S_Σ (%)	*A priori* BB.	Biomass burning RM	CSW	PNW	Total	Anth.	Total
A priori									1.3	0.5	1.0	2.8	5.8	8.6
A posteriori	**Analytical**		2°×2.5°	69	500	50	30	2.8	7.6	1.4	0.9	9.9 (3.5[b])	2.8 (0.5)	12.7 (1.5)
			0.5°×0.667°	69	500	50	30	2.8	4.1	0.1	1.9	6.1 (2.7)	3.1 (0.5)	9.1 (1.1)
	Adjoint	**Case 1**	2°×2.5°	69	500	50	30	2.8	3.0	1.4	1.5	5.9 (2.1)	11.8 (2.0)	17.7 (2.1)
		Case 2	2°×2.5°	69	300	50	30	2.8	2.9	1.3	1.4	5.6 (2.0)	11.6 (2.0)	17.2 (2.0)
		Case 3	2°×2.5°	69	500	30	30	2.8	3.2	1.4	1.6	6.2 (2.2)	11.4 (2.0)	17.6 (2.0)
		Case 4	2°×2.5°	69	500	200	30	2.8	3.3	1.5	1.7	6.5 (2.3)	12.8 (2.2)	19.3 (2.2)
		Case 5	2°×2.5°	69	500	50	100	2.8	2.4	1.2	1.0	4.6 (1.7)	10.3 (1.8)	14.9 (1.7)
		Case 6	2°×2.5°	56	500	50	30	2.8	2.8	1.3	1.4	5.5 (2.0)	11.1 (1.9)	16.6 (1.9)
		Case 7	2°×2.5°	69	200	200	30	2.8	3.1	1.4	1.5	6.0 (2.2)	12.5 (2.2)	18.5 (2.2)
		Case 8	2°×2.5°	69	500	50	30	3.0[c]	3.1	1.4	1.5	6.0 (2.1)	11.6 (2.0)	17.6 (2.0)
		Case 9	0.5°×0.667°	69	500	50	30	2.8	2.2	0.8	2.3	5.3 (1.9)	8.6 (1.5)	13.9 (1.6)

[a]See Fig. 1 in Mao et al. (2014) for the geographical definitions of the BC source regions.
[b]Scaling factors are in parentheses.
[c]The *a priori* biomass burning emissions uniformly increased by 2.5 Mg in every model grid box.

Table 2. Monthly anthropogenic and biomass burning emissions of BC (unit: Gg) in the WUS from the adjoint inversions for August 2006 using pseudo observations.

		Inversion configurations			Emissions (Gg (10^9 g))			J(x) reduction[c] (%)
		Pseudo observations	S_aANTH (%)	S_aBB (%)	Anth.	BB	Δ Emissions[b]	
A posteriori	**Pseudo 1**	every surface grid box	50	500	7.7 (1.3[a])	6.5 (2.3)	5.6 (2.0)	95
	Pseudo 2	every grid box in the lowest 15 layers	50	500	7.8 (1.3)	6.4 (2.3)	5.6 (2.0)	97
	Pseudo 3	every surface grid box	10	500	7.1 (1.2)	6.9 (2.5)	5.4 (1.9)	95
	Pseudo 4	every surface grid box	0	500	5.8 (1.0)	8.2 (2.9)	5.4 (1.9)	99
	Pseudo 5	every surface grid box	50	0	10.0 (1.7)	2.8 (1.0)	4.2 (1.5)	55
	Pseudo 6	randomly in 75% of the surface grid boxes	50	500	7.8 (1.3)	6.2 (2.2)	5.4 (1.9)	94
	Pseudo 7	randomly in 50% of the surface grid boxes	50	500	8.0 (1.4)	5.9 (2.1)	5.3 (1.9)	93
	Pseudo 8	randomly in 25% of the surface grid boxes	50	500	7.5 (1.3)	5.3 (1.9)	4.2 (1.5)	96
	Pseudo 9	in the surface grid boxes with fire counts (> 5)	50	500	7.6 (1.3)	6.2 (2.2)	5.2 (1.9)	95
'Ghost' emissions[d]					5.8 (1.0)	8.4 (3.0)	5.6 (2.0)	
A priori					5.8	2.8		

[a]Scaling factors in parentheses.
[b]The increase of total emissions relative to the *a priori* biomass burning emissions (ratio of the total emissions change over the *a priori* biomass burning emissions in parentheses).
[c]The reduction of the *a posteriori* cost function relative to the *a priori*.
[d]Emissions (with anthropogenic emissions unchanged but biomass burning emissions tripled) used to generate the pseudo observations for Pseudos 1-9.

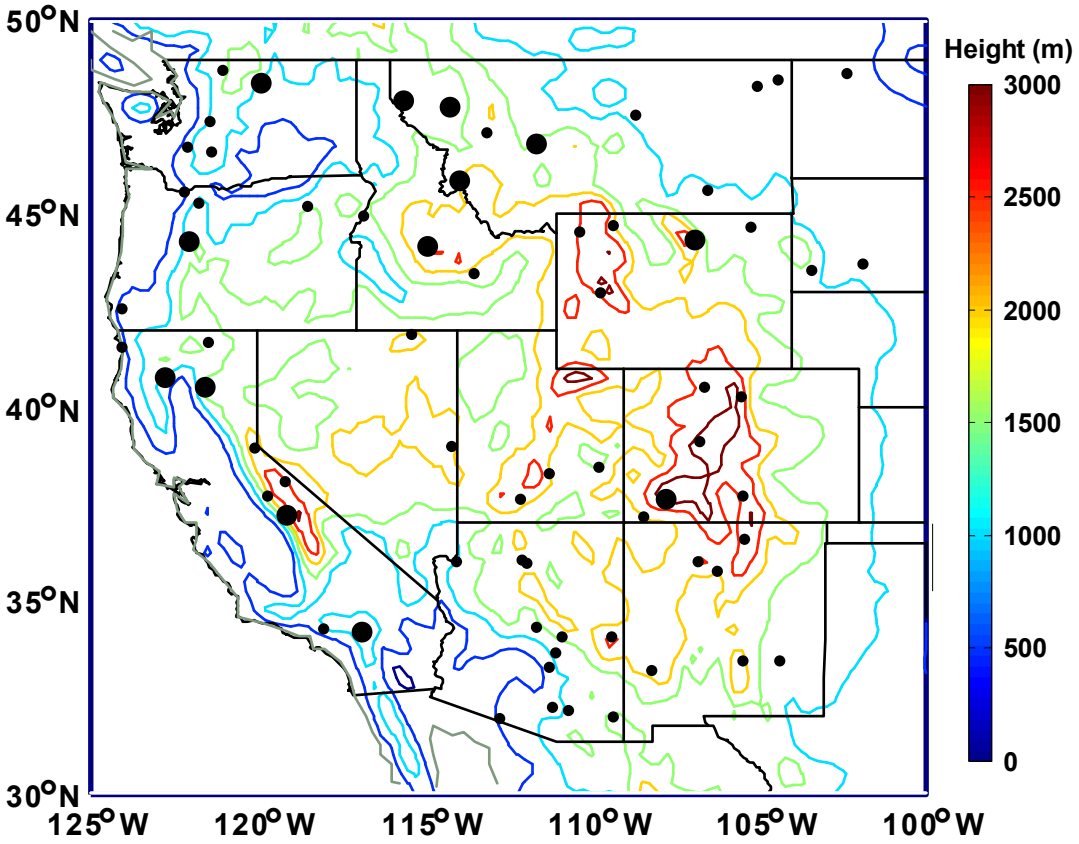
50°N
45°N
40°N
35°N
30°N
125°W
120°W
115°W
110°W
105°W
100°W
Height (m)
3000
2500
2000
1500
1000
500
0

Fig. 1

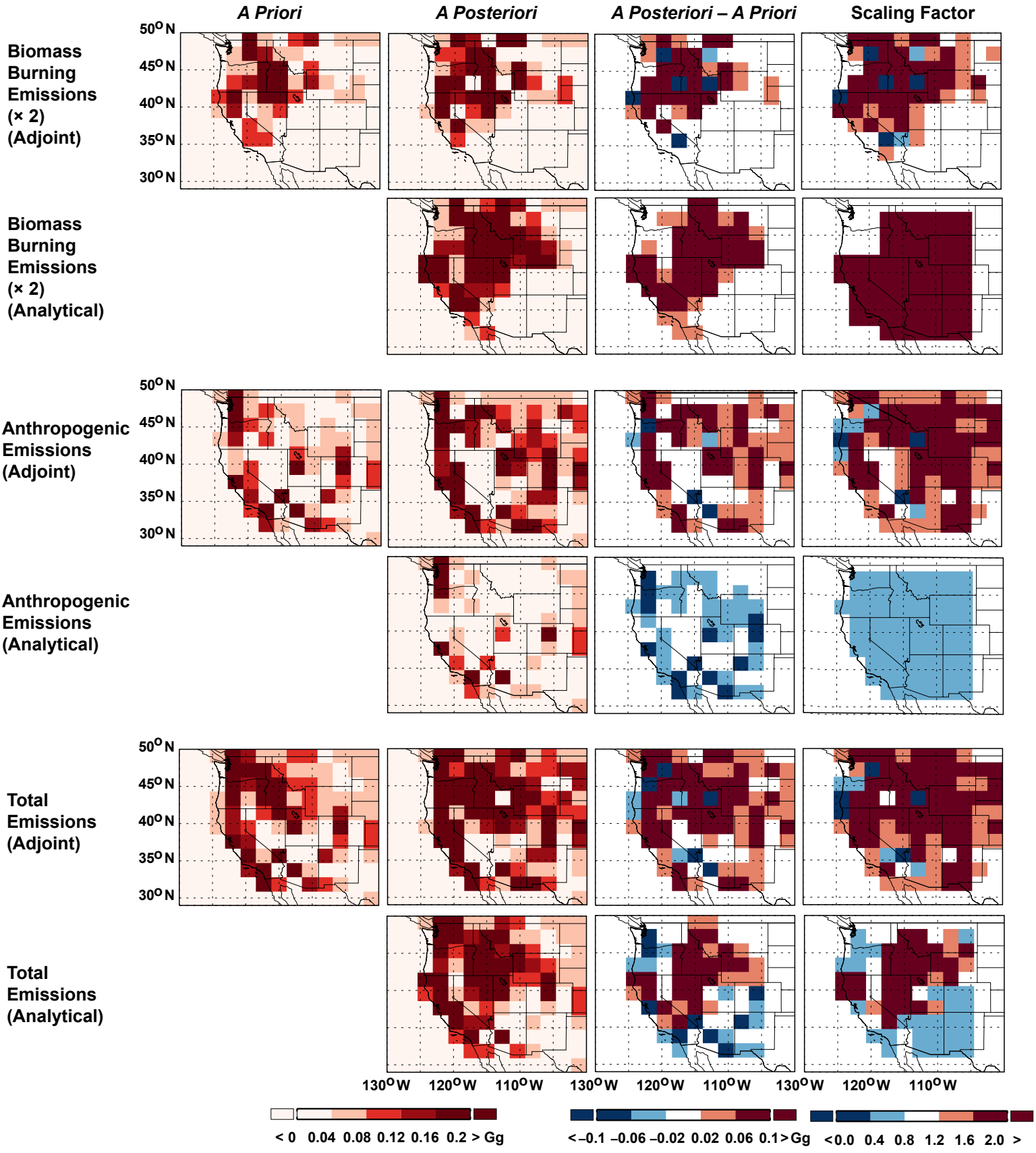
A Priori
A Posteriori
A Posteriori – A Priori
Scaling Factor
Biomass Burning Emissions (× 2) (Adjoint)
Biomass Burning Emissions (× 2) (Analytical)
Anthropogenic Emissions (Adjoint)
Anthropogenic Emissions (Analytical)
Total Emissions (Adjoint)
Total Emissions (Analytical)
50°N
45°N
40°N
35°N
30°N
130°W
120°W
110°W
< 0 0.04 0.08 0.12 0.16 0.2 > Gg
< –0.1 –0.06 –0.02 0.02 0.06 0.1 > Gg
< 0.0 0.4 0.8 1.2 1.6 2.0 >

Fig. 2.

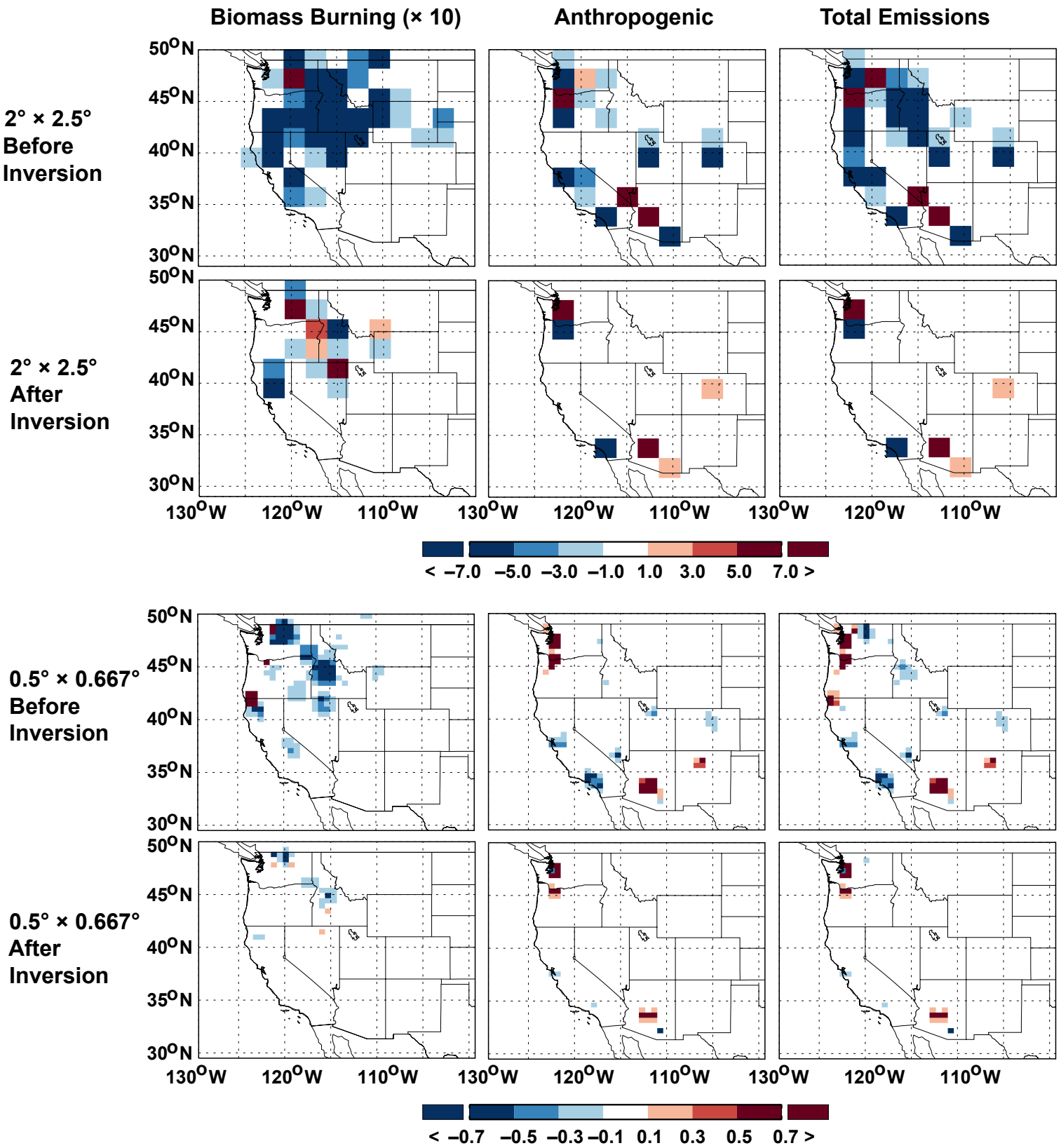
Biomass Burning (× 10)
Anthropogenic
Total Emissions
2° × 2.5° Before Inversion
2° × 2.5° After Inversion
0.5° × 0.667° Before Inversion
0.5° × 0.667° After Inversion
50°N
45°N
40°N
35°N
30°N
130°W
120°W
110°W
< –7.0 –5.0 –3.0 –1.0 1.0 3.0 5.0 7.0 >
< –0.7 –0.5 –0.3 –0.1 0.1 0.3 0.5 0.7 >

Fig. 3.

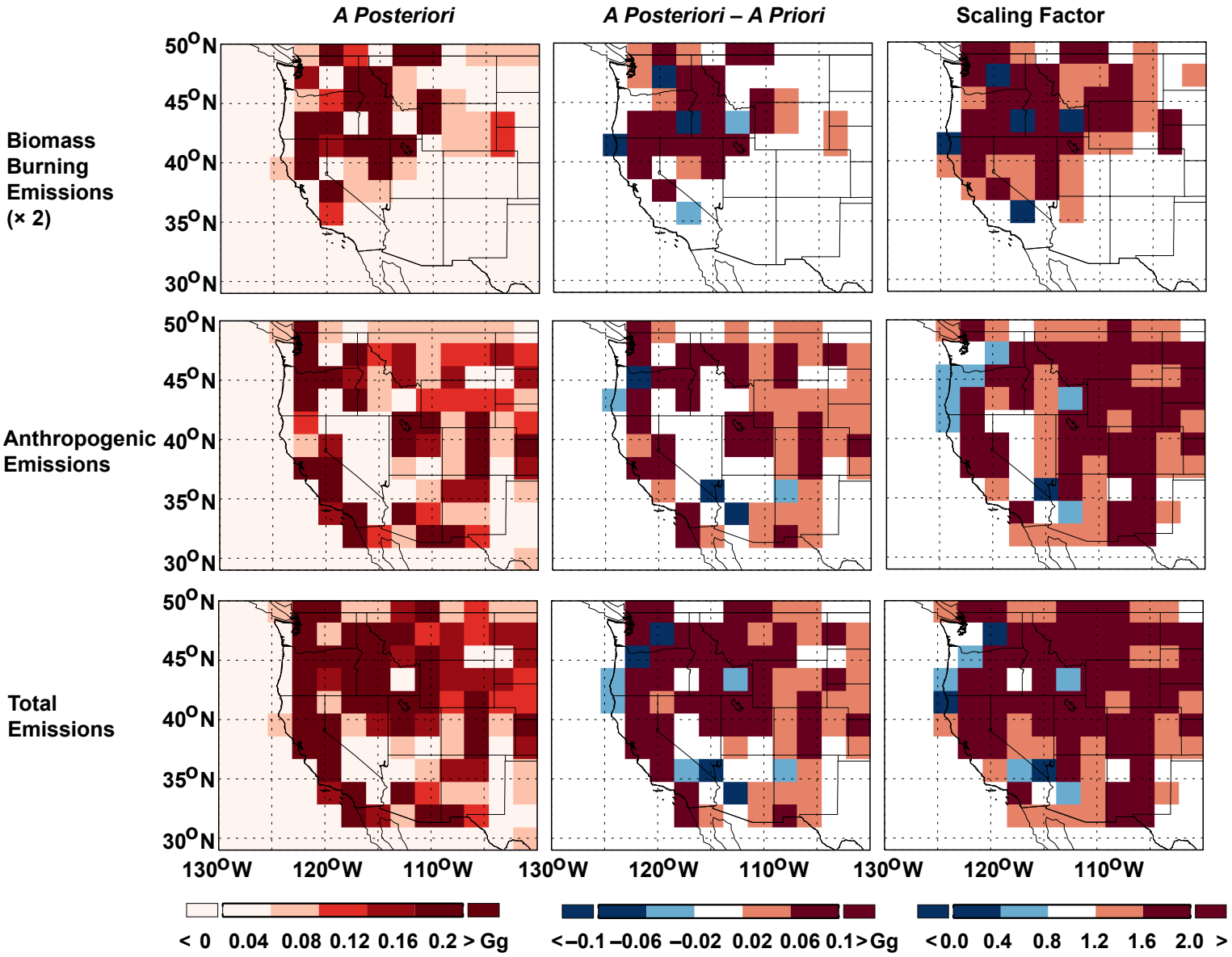
A Posteriori
A Posteriori – A Priori
Scaling Factor
Biomass Burning Emissions (× 2)
Anthropogenic Emissions
Total Emissions
50°N
45°N
40°N
35°N
30°N
130°W
120°W
110°W
< 0 0.04 0.08 0.12 0.16 0.2 > Gg
<–0.1 –0.06 –0.02 0.02 0.06 0.1> Gg
<0.0 0.4 0.8 1.2 1.6 2.0 >

Fig. 4.

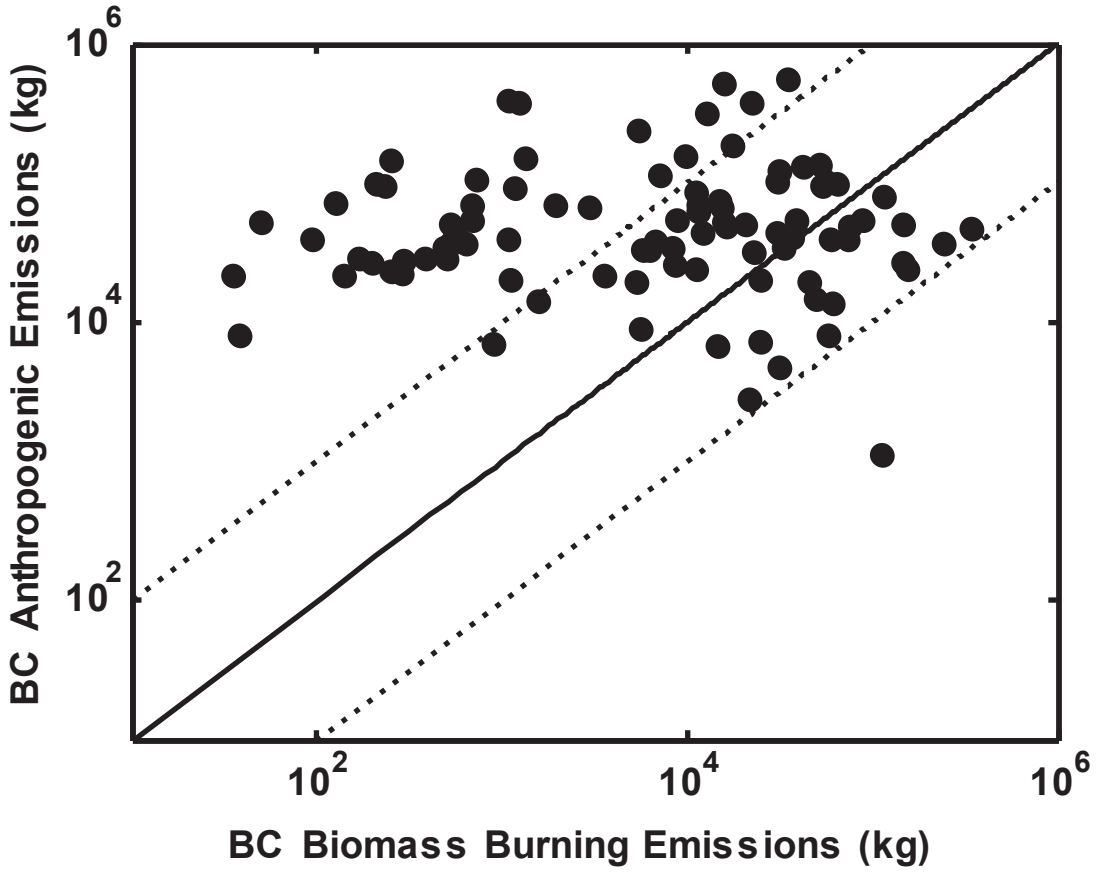
BC Anthropogenic Emissions (kg)
10^6
10^4
10^2
10^2
10^4
10^6
BC Biomass Burning Emissions (kg)

Fig. 5

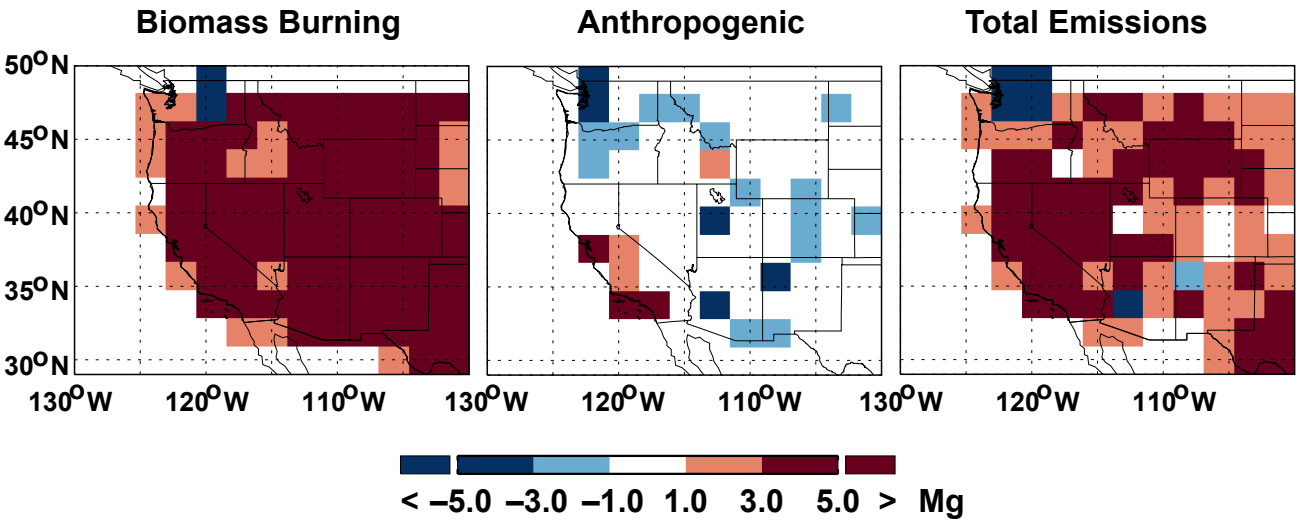
Biomass Burning
Anthropogenic
Total Emissions
50°N
45°N
40°N
35°N
30°N
130°W
120°W
110°W
< –5.0 –3.0 –1.0 1.0 3.0 5.0 > Mg

Fig. 6.

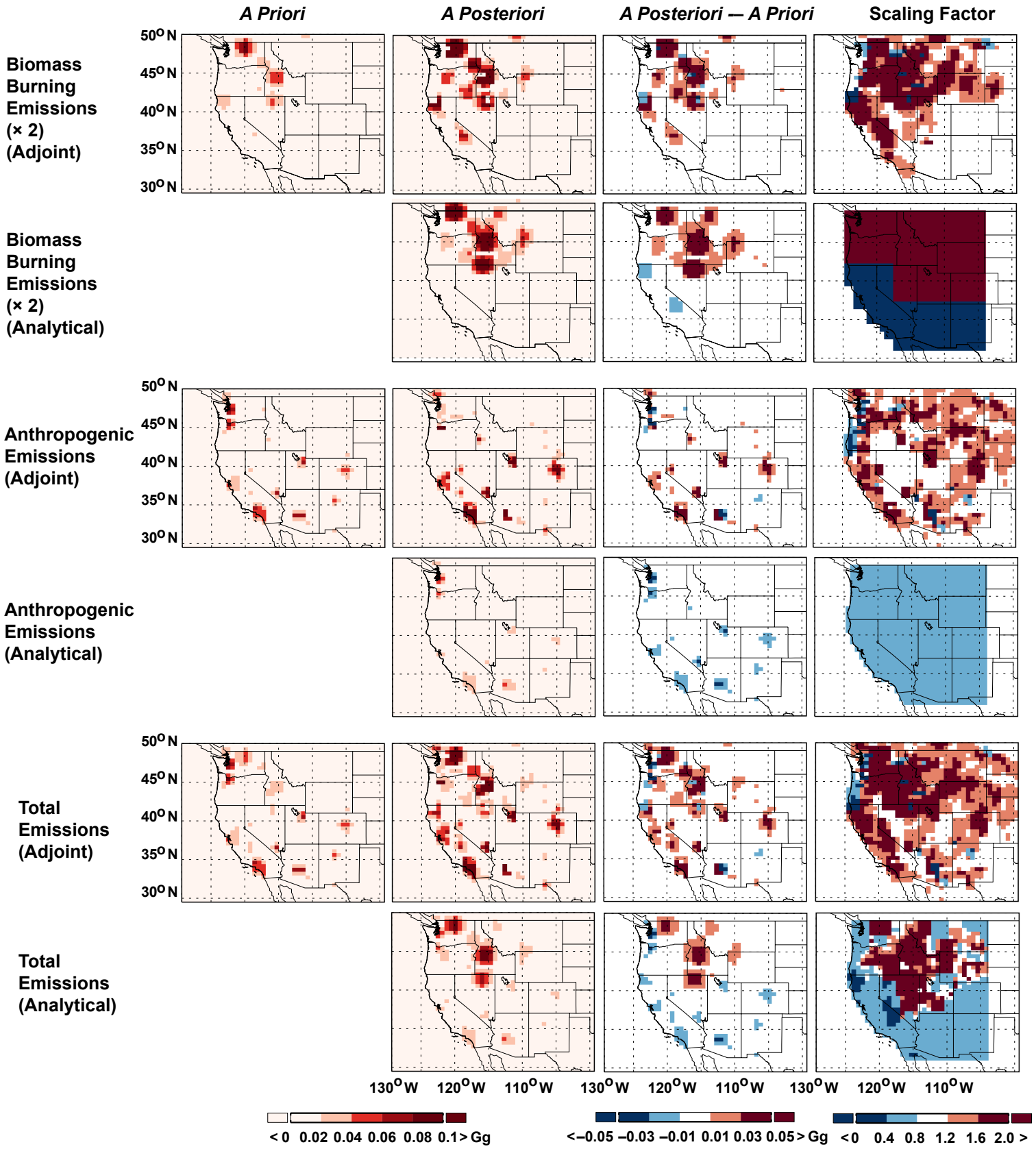
A Priori
A Posteriori
A Posteriori — A Priori
Scaling Factor
Biomass Burning Emissions (× 2) (Adjoint)
Biomass Burning Emissions (× 2) (Analytical)
Anthropogenic Emissions (Adjoint)
Anthropogenic Emissions (Analytical)
Total Emissions (Adjoint)
Total Emissions (Analytical)
50° N
45° N
40° N
35° N
30° N
130° W
120° W
110° W
< 0 0.02 0.04 0.06 0.08 0.1 > Gg
< –0.05 –0.03 –0.01 0.01 0.03 0.05 > Gg
< 0 0.4 0.8 1.2 1.6 2.0 >

Fig. 7.

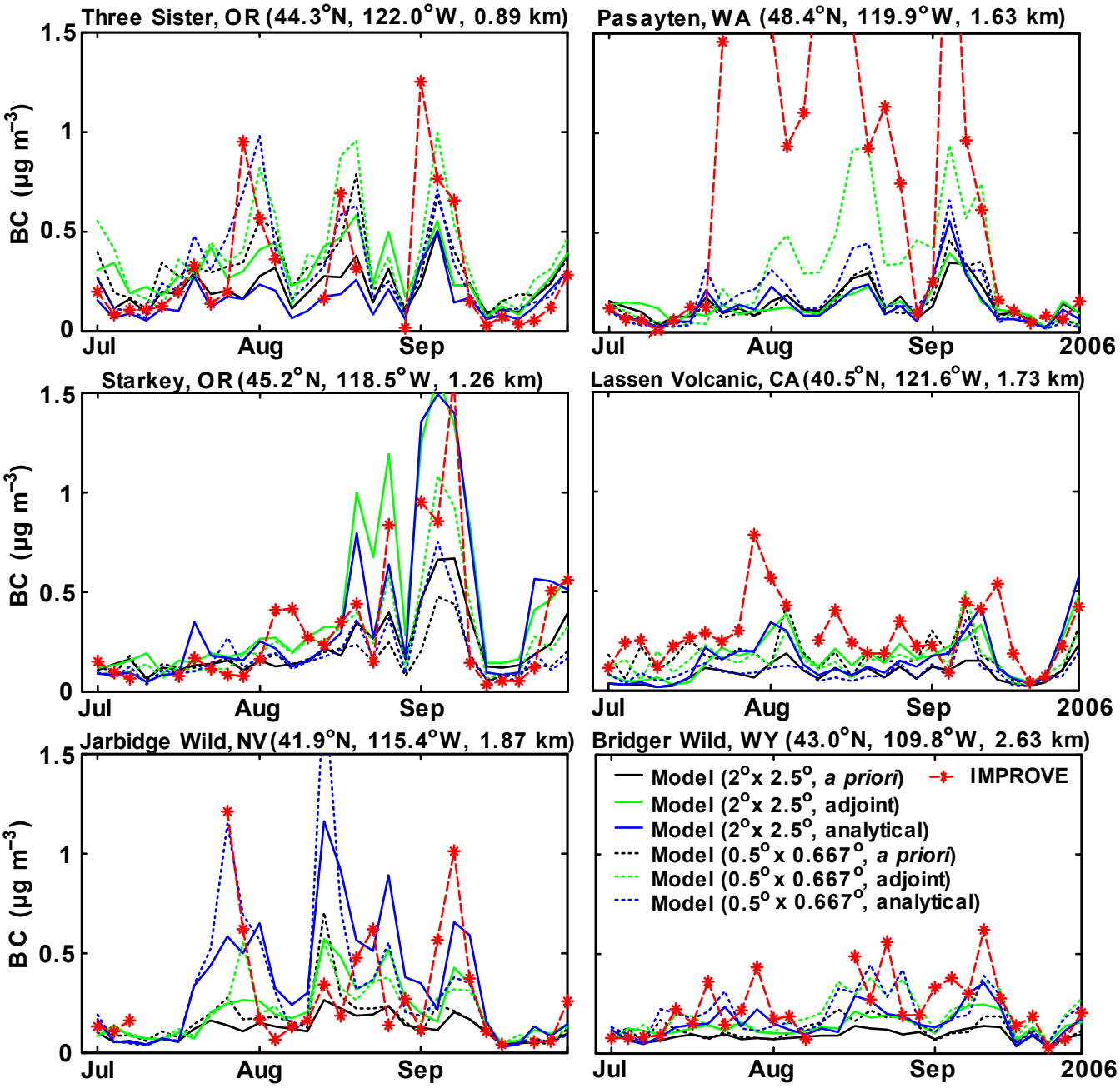
Three Sister, OR (44.3°N, 122.0°W, 0.89 km)
Pasayten, WA (48.4°N, 119.9°W, 1.63 km)
Starkey, OR (45.2°N, 118.5°W, 1.26 km)
Lassen Volcanic, CA (40.5°N, 121.6°W, 1.73 km)
Jarbidge Wild, NV (41.9°N, 115.4°W, 1.87 km)
Bridger Wild, WY (43.0°N, 109.8°W, 2.63 km)
BC (μg m−3)
0
0.5
1
1.5
Jul
Aug
Sep
2006
Model (2°x 2.5°, a priori)
Model (2°x 2.5°, adjoint)
Model (2°x 2.5°, analytical)
Model (0.5°x 0.667°, a priori)
Model (0.5°x 0.667°, adjoint)
Model (0.5° x 0.667°, analytical)
IMPROVE

Fig. 8

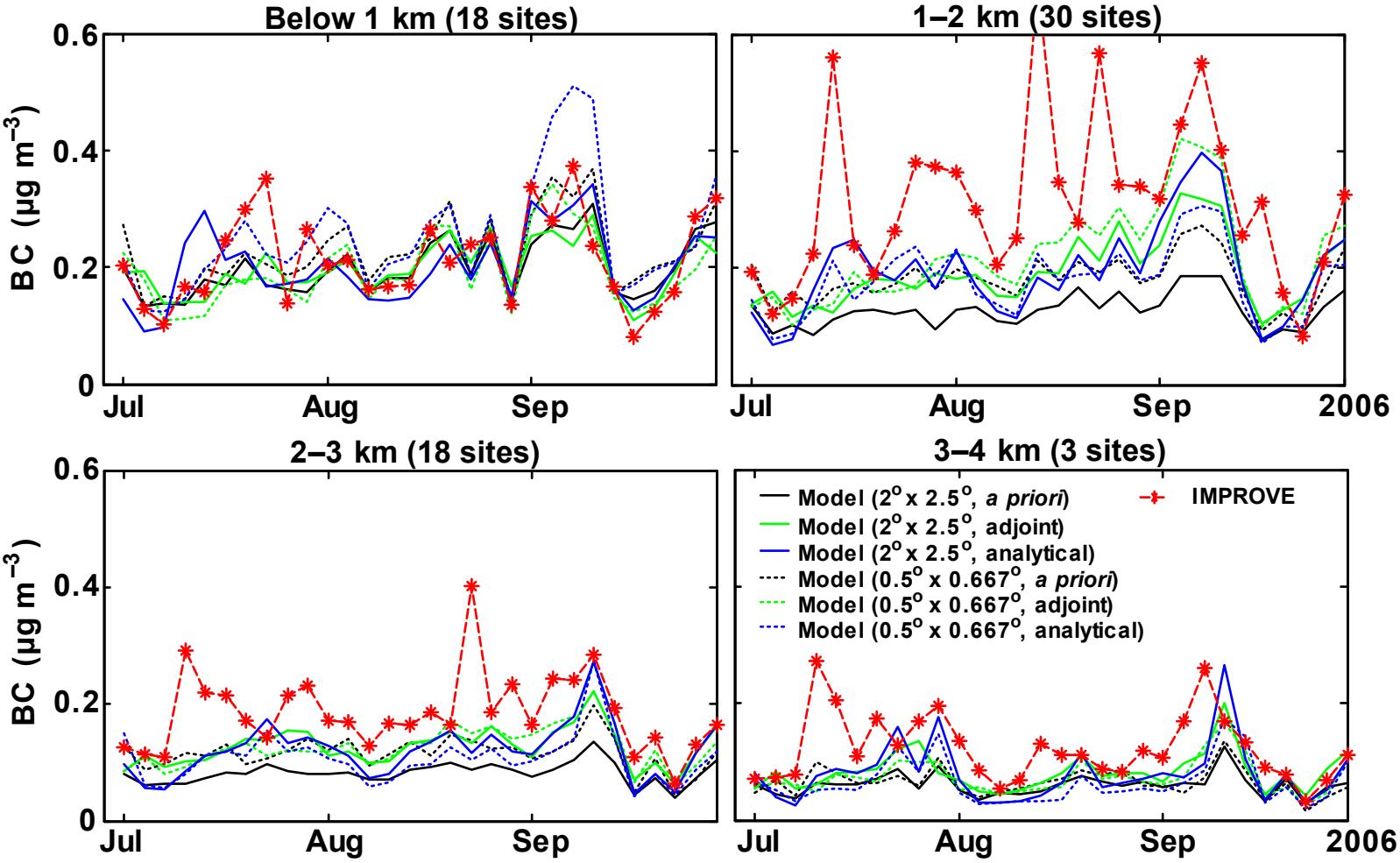
Below 1 km (18 sites)
1–2 km (30 sites)
2–3 km (18 sites)
3–4 km (3 sites)
BC (μg m−3)
0
0.2
0.4
0.6
Jul
Aug
Sep
2006
Model (2° x 2.5°, a priori)
Model (2° x 2.5°, adjoint)
Model (2° x 2.5°, analytical)
Model (0.5° x 0.667°, a priori)
Model (0.5° x 0.667°, adjoint)
Model (0.5° x 0.667°, analytical)
IMPROVE

Fig. 9

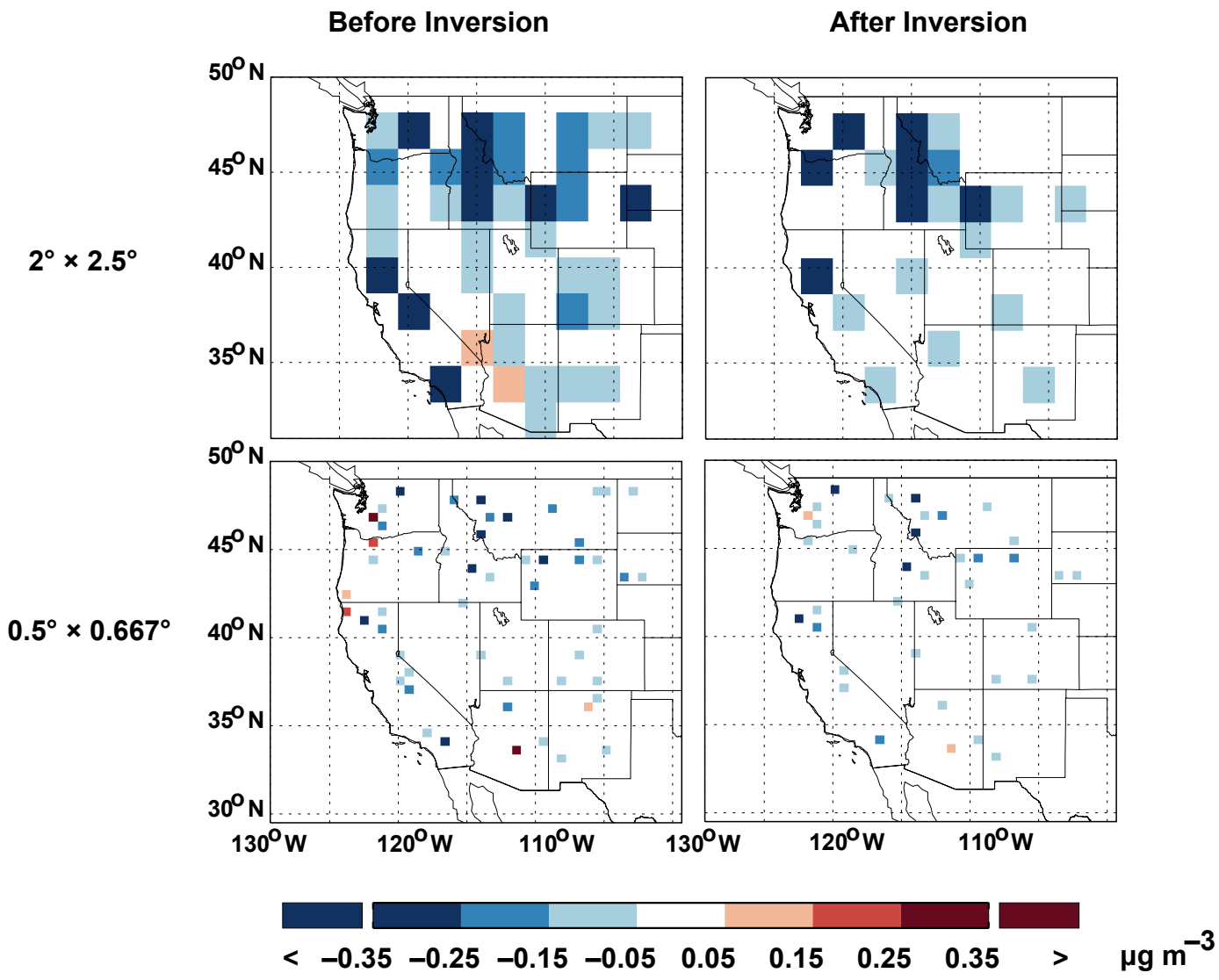
Before Inversion
After Inversion
2° × 2.5°
0.5° × 0.667°
50°N
45°N
40°N
35°N
30°N
130°W
120°W
110°W
< –0.35 –0.25 –0.15 –0.05 0.05 0.15 0.25 0.35 >
μg m–3

Fig. 10.

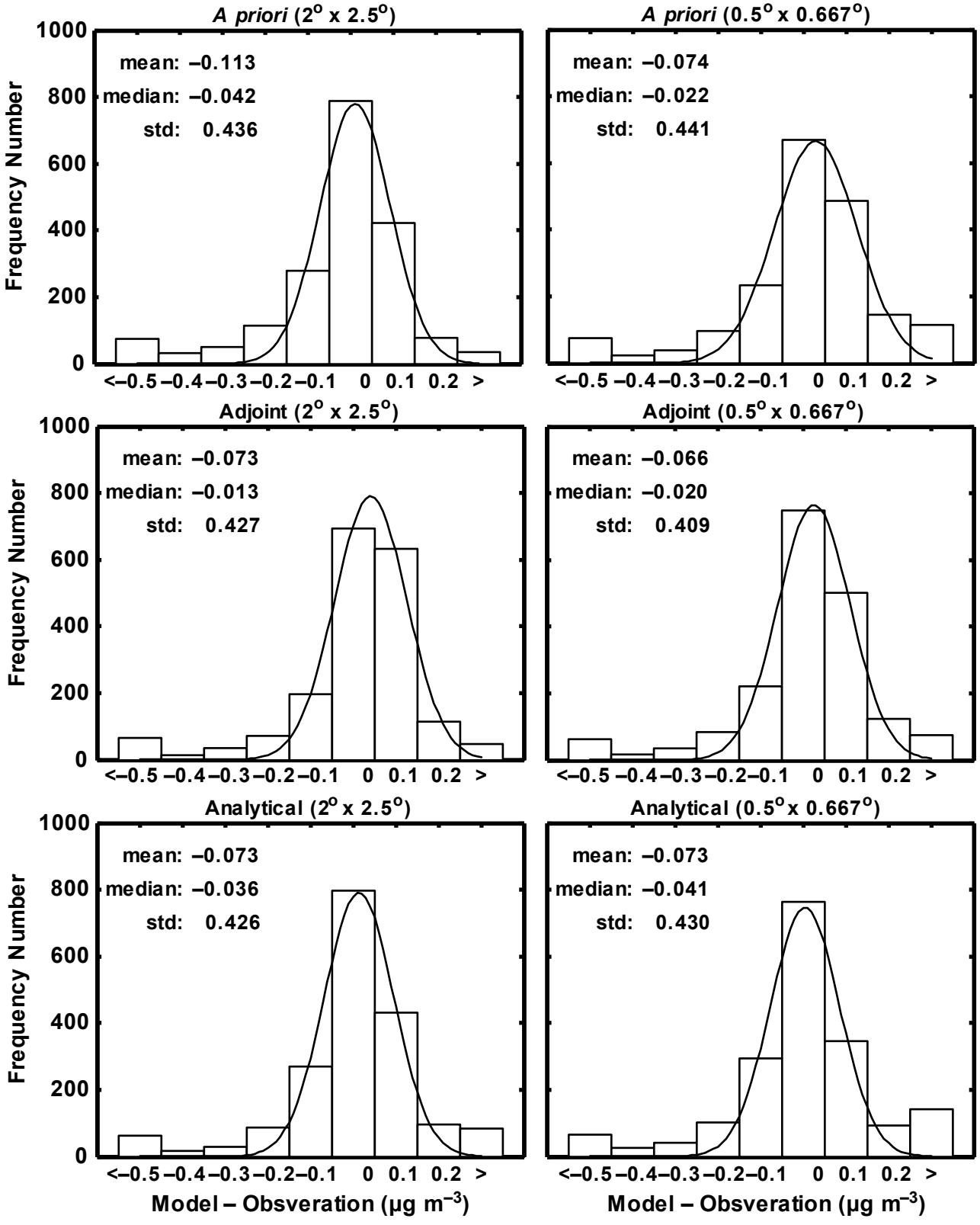
A priori (2° x 2.5°)
mean: –0.113
median: –0.042
std: 0.436
A priori (0.5° x 0.667°)
mean: –0.074
median: –0.022
std: 0.441
Adjoint (2° x 2.5°)
mean: –0.073
median: –0.013
std: 0.427
Adjoint (0.5° x 0.667°)
mean: –0.066
median: –0.020
std: 0.409
Analytical (2° x 2.5°)
mean: –0.073
median: –0.036
std: 0.426
Analytical (0.5° x 0.667°)
mean: –0.073
median: –0.041
std: 0.430
Frequency Number
0
200
400
600
800
1000
<–0.5 –0.4 –0.3 –0.2 –0.1 0 0.1 0.2 >
Model – Obsveration (μg m–3)

Fig. 11

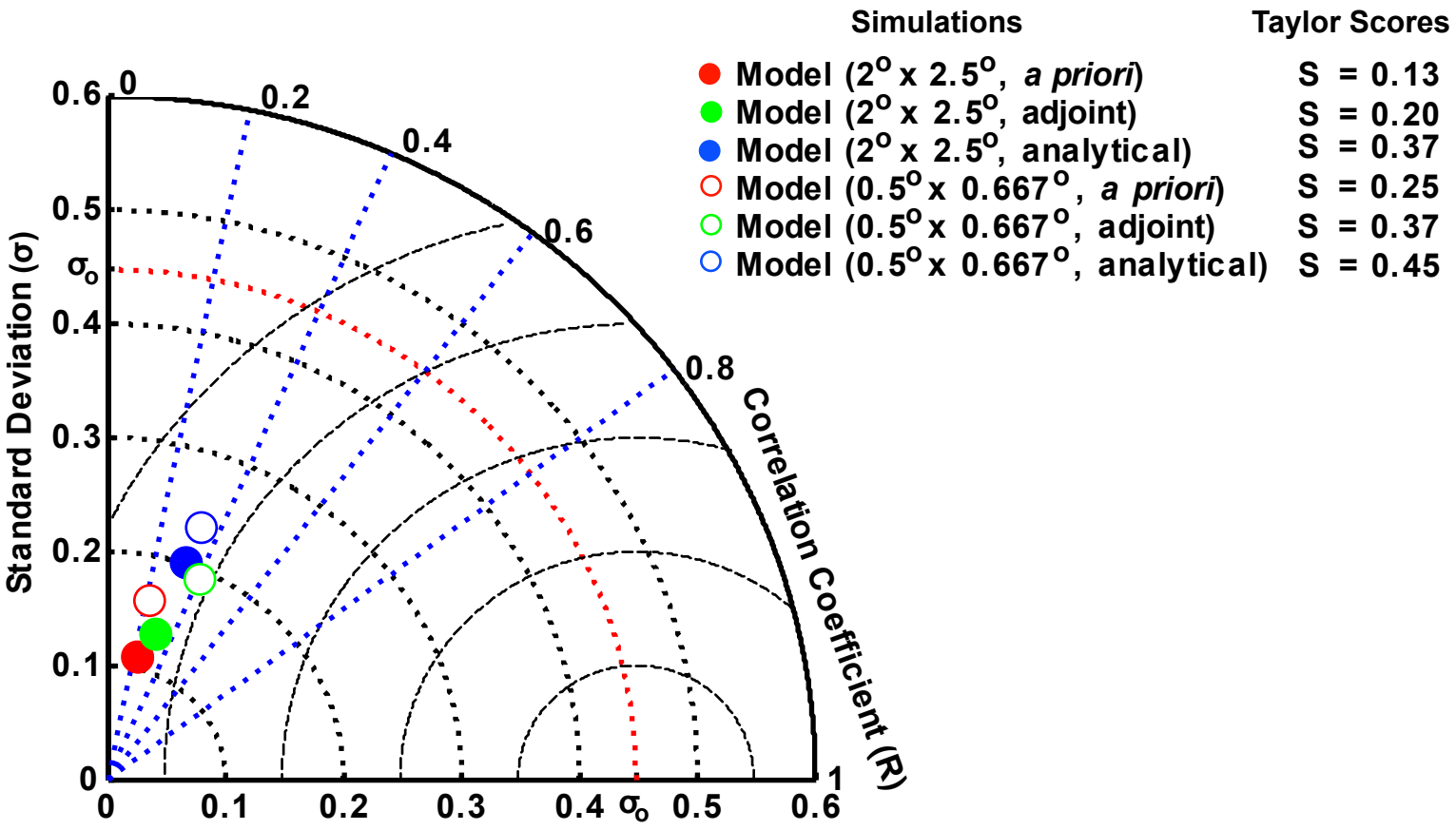
Simulations
Taylor Scores
Model (2° x 2.5°, a priori) S = 0.13
Model (2° x 2.5°, adjoint) S = 0.20
Model (2° x 2.5°, analytical) S = 0.37
Model (0.5° x 0.667°, a priori) S = 0.25
Model (0.5° x 0.667°, adjoint) S = 0.37
Model (0.5° x 0.667°, analytical) S = 0.45
Standard Deviation (σ)
Correlation Coefficient (R)
σo
0
0.2
0.4
0.6
0.8
1
0.1
0.3
0.5

Fig. 12

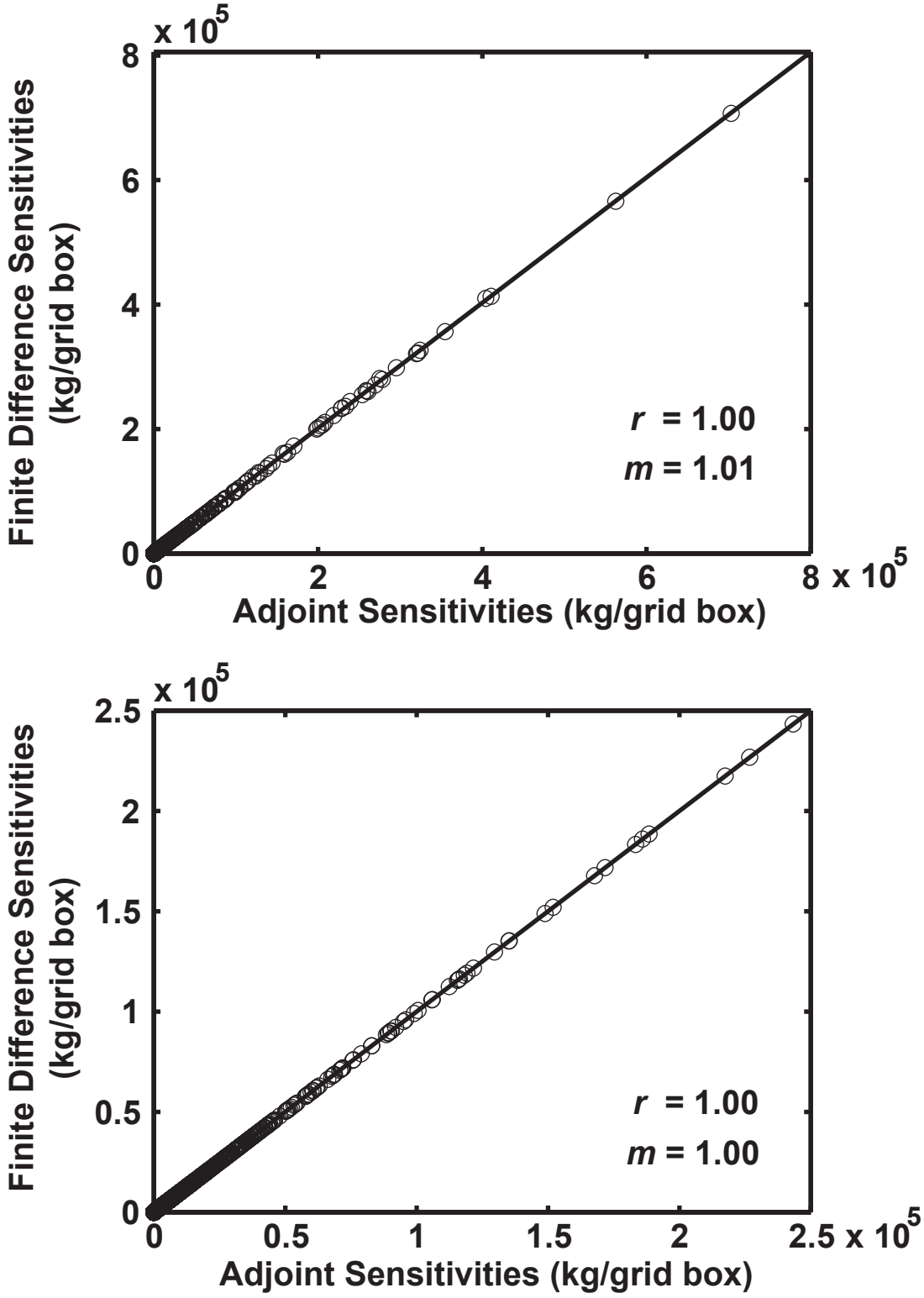
x 10^5
8
6
4
2
0
Finite Difference Sensitivities (kg/grid box)
r = 1.00
m = 1.01
0
2
4
6
8 x 10^5
Adjoint Sensitivities (kg/grid box)
x 10^5
2.5
2
1.5
1
0.5
0
Finite Difference Sensitivities (kg/grid box)
r = 1.00
m = 1.00
0
0.5
1
1.5
2
2.5 x 10^5
Adjoint Sensitivities (kg/grid box)

Fig. S1

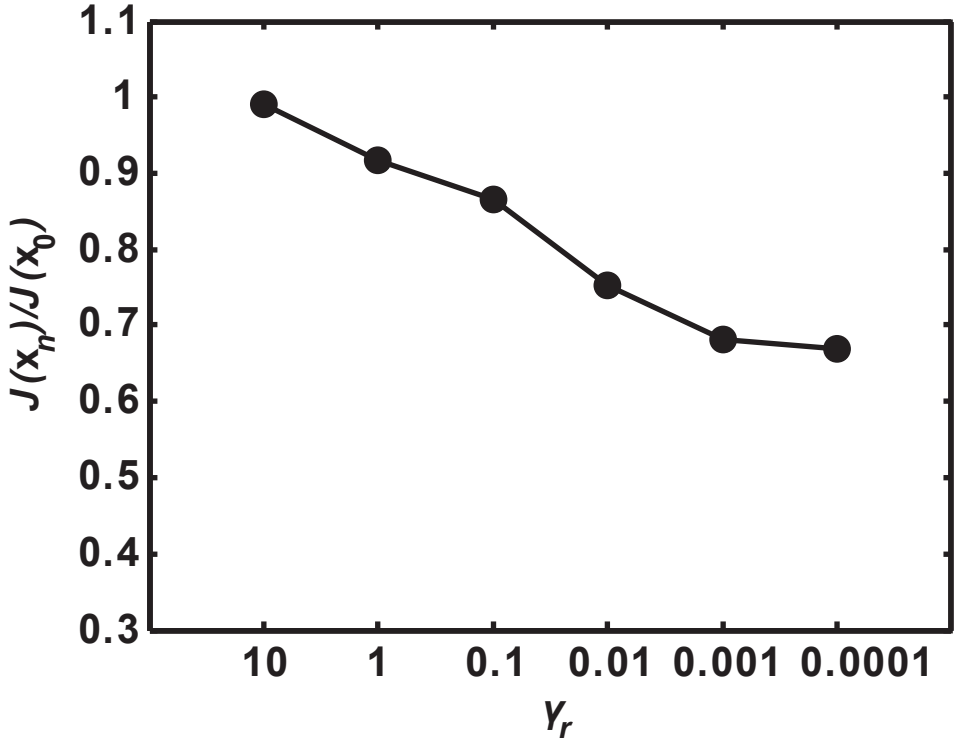
1.1
1
0.9
0.8
0.7
0.6
0.5
0.4
0.3
$J(x_n)/J(x_0)$
10
1
0.1
0.01
0.001
0.0001
γ_r

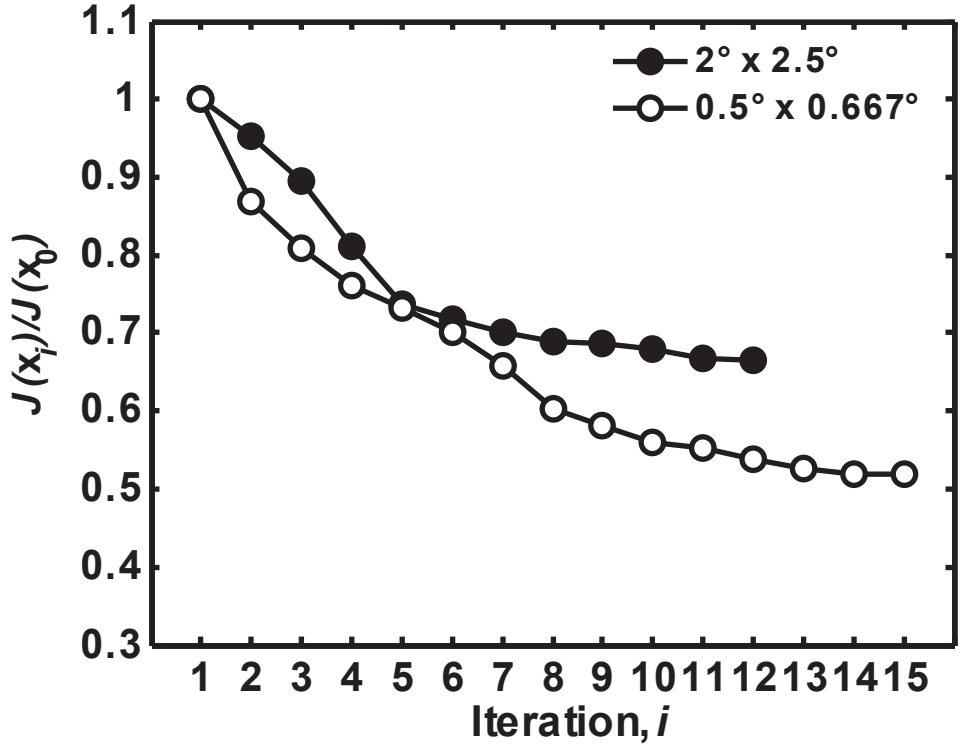
1.1
1
0.9
0.8
0.7
0.6
0.5
0.4
0.3
$J(x_i)/J(x_0)$
2° x 2.5°
0.5° x 0.667°
1 2 3 4 5 6 7 8 9 10 11 12 13 14 15
Iteration, i

Fig. S2